

Controlling Infectious Disease: Prevention and Intervention Through Multiscale Models

Aдриенна Бингем

Сан Анхело, Техас

Master of Science, College of William & Mary, 2016

Bachelor of Science, Angelo State University, 2014

A Dissertation presented to the Graduate Faculty
of The College of William & Mary in Candidacy for the Degree of
Doctor of Philosophy

Department of Applied Science

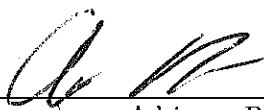
College of William & Mary
August 2019

©
Adrienna Bingham
All rights reserved.

APPROVAL PAGE

This Dissertation is submitted in partial fulfillment of
the requirements for the degree of

Doctor of Philosophy

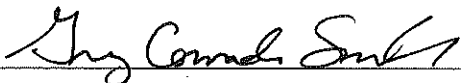


Adrienna Bingham

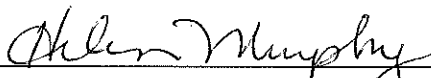
Approved by the Committee, June 2019



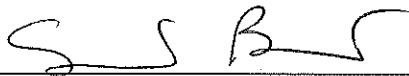
Committee Chair
Associate Professor Leah B. Shaw, Mathematics
College of William & Mary



Professor Gregory Conradi-Smith, Applied Science
College of William & Mary



Assistant Professor Helen Murphy, Biology
College of William & Mary



Dr. Simone Bianco, Industrial and Applied Genomics
IBM Almaden Research Center

ABSTRACT

Controlling infectious disease spread and preventing disease onset are ongoing challenges, especially in the presence of newly emerging diseases. While vaccines have successfully eradicated smallpox and reduced occurrence of many diseases, there still exists challenges such as fear of vaccination, the cost and difficulty of transporting vaccines, and the ability of attenuated viruses to evolve, for instance leading to vaccine derived poliovirus.

Antibiotic resistance due to mistreatment of antibiotics and quickly evolving bacteria contributes to the difficulty of eradicating diseases such as tuberculosis. Additionally, bacteria and fungi are able to produce an extracellular matrix in biofilms that protects them from antibiotics/antifungals.

Mathematical models are an effective way of measuring the success of various control measures, allowing for cost savings and efficient implementation of those measures. While many models exist to investigate the dynamics on a human population scale, it is also beneficial to use models on a microbial scale to further capture the biology behind infectious diseases. In this dissertation, we develop mathematical models at several spatial scales to help improve disease control.

At the scale of human populations, we develop differential equation models with quarantine control. We investigate how the distribution of exposed and infectious periods affects the control efficacy and suggest when it is important for models to include realistically narrow distributions.

At the microbial scale, we use an agent-based stochastic spatial simulation to model the social interactions between two yeast strains in a biofilm. While cheater strains have been proposed as a control strategy to disrupt the harmful cooperative biofilm, some yeast strains cooperate only with other cooperators via kin recognition. We study under what circumstances kin recognition confers the greatest fitness benefit to a cooperative strain. Finally, we look at a multiscale, two-patch model for the dynamics between wild-type (WT) poliovirus and defective interfering particles (DIPs) as they travel between organs. DIPs are non-viable variants of the WT that lack essential elements needed for reproduction, causing them to steal these elements from the WT. We investigate when DIPs can lower the WT population in the host.

TABLE OF CONTENTS

| | |
|--|----|
| Acknowledgments | iv |
| Dedication | v |
| Chapter | |
| 1 Introduction | 1 |
| 1.1 Forms of Control | 2 |
| 1.2 Mathematical Modeling | 3 |
| 2 Applying Quarantine to Infectious: Does Ignoring Time Delay Lead to Incorrect Predictions? | 6 |
| 2.1 Introduction | 6 |
| 2.2 Models | 8 |
| 2.3 Steady States and Basic Reproduction Numbers | 13 |
| 2.3.1 Exponential Model | 13 |
| 2.3.2 Delay Differential Equation Model | 14 |
| 2.3.3 Multi-Infected Compartment Model | 15 |
| 2.4 Example of Underestimation of Infectious Population in Exponential System | 17 |
| 2.5 Effect of Number of Compartments on Infectious Steady State | 19 |
| 2.6 Effect of Length of Time Delay on Infectious Steady State | 23 |
| 2.7 Effects of Different Control Applications | 25 |
| 2.8 Conclusion | 27 |
| 2.9 Appendix | 30 |
| 2.9.1 Endemic Steady State for Exponential System | 30 |
| 2.9.2 Endemic Steady State for Delay System | 30 |
| 2.9.3 R_0 for Multi-Infected Compartment Model | 31 |
| 2.9.4 Infectious Steady State with Applying Vaccine on Susceptible Class | 34 |
| 2.9.5 Infectious Steady States with Applying Quarantine on Exposed Class | 34 |

| | | |
|-------|---|----|
| 3 | The Effect of Kin Recognition on Competition Among Clones in Spatially Structured Microbial Communities | 35 |
| 3.1 | Introduction | 35 |
| 3.2 | Methods | 38 |
| 3.3 | Results | 43 |
| 3.3.1 | Total Proportion of Cooperators | 43 |
| 3.3.2 | Benefit to Relatedness | 44 |
| 3.3.3 | Sparse Versus Dense Colonies | 45 |
| 3.4 | Conclusion | 47 |
| 3.5 | Appendix | 48 |
| 3.5.1 | Calculating the Occupancy Fractions | 48 |
| 3.5.2 | Finding an Empty Site and Cell Movement | 49 |
| 3.5.3 | Total Proportion of Cooperators in Various Colony Densities | 51 |
| 4 | Two-Patch Organ Model for Competition Between Defective Interfering Particles and Wild-Type Poliovirus | 52 |
| 4.1 | Introduction | 52 |
| 4.2 | Methods | 54 |
| 4.3 | Results | 57 |
| 4.3.1 | Stability analysis of disease free equilibrium | 57 |
| 4.3.2 | Simulations | 58 |
| 4.3.3 | Effect of Parameters on DIP Intervention | 62 |
| 4.3.4 | Bifurcation Analysis | 64 |
| 4.4 | Conclusion | 66 |
| 4.5 | Appendix | 67 |
| 4.5.1 | Eigenvalues of the Disease Free State | 67 |
| 4.5.2 | Changing Bottleneck to Prolong Delay to Organ B | 68 |
| 4.5.3 | Simulation Figures | 69 |
| 4.5.4 | Delaying DIP Intervention | 70 |

| | |
|------------------------|----|
| 5 Epilogue | 72 |
| Bibliography | 74 |
| Vita | 82 |

ACKNOWLEDGMENTS

I would like to thank my advisor, Dr. Leah Shaw, for her support and mentorship throughout this Ph.D. I would also like to thank my committee members, Dr. Helen Murphy, Dr. Greg Conradi-Smith, and Dr. Simone Bianco. I would like to thank all my friends who were supportive throughout this journey, especially Sofya Zaytseva and Laura Dickinson. I am especially grateful for my family: my parents, Ronny and Laura, and my sisters, Rebecca and Marissa, for having Christmases in January, for using their vacations to visit Williamsburg, for standing by me, and for encouraging me the whole way.

This dissertation is dedicated to my family, who gave me the encouragement to never give up. I love you guys.

Chapter 1

Introduction

Infectious diseases have always been a part of human life, affecting the way we live, how we communicate, and even our politics (Sherman, 2007). While some infections may not be contagious or are simple colds, some diseases have wiped out whole populations. The Bubonic plague from 1346-1352 killed so much of Europe's population, it took over 150 years for it to return to its previous size (Sherman, 2007). During the 17th century, Smallpox disfigured or killed about 400,000 Europeans every year. The Spanish flu (the Great Influenza) of 1918 killed more than 22 million people in two years (Brauer et al., 2001; Sherman, 2007). Although not contagious by human contact, the fungus *Phytophthora infestans* caused the Irish Potato Famine, reducing the Irish population by over 2 million, whether through death or emigration.

Infections can be caused by various agents. Virus particles lead to diseases such as poliovirus, smallpox, Ebola, and HIV (Sherman, 2007). Bacteria can cause food poisoning, form biofilms in the human body leading to infection (West et al., 2007), and lead to outbreaks of cholera (Sherman, 2007). Agents can be non-contagious or contagious. When contagious, they can spread from person to person through direct skin contact, through the transfer of bodily fluids, or through the air. They can even be transferred from animal vectors such as malaria via mosquitoes (Sherman, 2007).

1.1 Forms of Control

Controlling the spread of disease has always been a challenge. Hospitals to treat the sick were created in the Middle East in about the 10th century and in Western Europe in 651 (Gaynes, 2011). The idea of quarantine first came around in the time of Hippocrates and Galen when they suggested that some diseases were “dangerous to associate with those afflicted” (Sherman, 2007). Before people knew the cause of cholera, they would keep cholera infested ships docked for a period to prevent the spread on land (Sherman, 2007). Later, vaccinations became a preventative measure, even eliminating smallpox (Sherman, 2007; Anderson et al., 1992). Agencies such as the CDC and WHO were created to continue the fight against infectious diseases. The CDC was created in 1946 by Dr. Joseph Mountin to have a headquarters for the fight against malaria (Centers for Disease Control and Prevention, 2018), while the WHO was created in 1948 as a result of a United Nations meeting (World Health Organization, 2019a).

These measures have their benefits. However, with the continued misuse of antibiotics, and viruses and bacteria’s ability to quickly evolve, such measures are quickly becoming ineffective and more creative measures must be taken when fighting health concerns (Gaynes, 2011). For example, syphilis is becoming more drug resistant, and due to infected individuals quitting tuberculosis treatment early, tuberculosis is also becoming more drug resistant. When stopping a treatment early, remaining bacteria mutate to become drug resistant. These mutated bacteria can then spread to another individual (Sherman, 2007). One proposed method to fight antibiotic resistance is through exploiting microbial social interactions. One example where this could be useful is disrupting biofilm formation. Biofilms are communities of bacteria or fungus that are attached to a surface and are protected from outside threats, such as antibiotics, by an extracellular matrix (Nadell et al., 2008, 2016). The extracellular matrix is created by cells within the community. Therefore, these cells must cooperate with each other in to successfully protect themselves from being eliminated. However, these cooperative communities can be taken advantage of by cheaters, individuals who do not

use energy to produce the extracellular matrix, and therefore can outgrow the cooperators leading to biofilm disruption (Nadell et al., 2008; Brown et al., 2009). Studying these types of social interactions allows us to figure out ways to prevent infectious disease in humans by eliminating biofilms. For instance, Brown et al. (2009) et al. propose and model a strategy for using a cheater strain as a Trojan horse that is inserted into the biofilm and eliminates it from the inside.

Additionally, vaccines can be costly, difficult to develop and transport, and could create fear in a society such as with the vaccine for poliovirus (Sherman, 2007) and today's battle with measles. On top of this, some viruses, especially RNA viruses, quickly evolve leading to vaccine derived viruses. An example is poliovirus, a single-stranded RNA virus, can change from a weakened, or attenuated, version of the virus that is used in vaccinations to the highly contagious virus, or vaccine derived poliovirus. This makes eliminating poliovirus from some areas of the world a very difficult task (Sherman, 2007). HIV is also able to quickly adapt and evolve as well. One method scientists are taking to attempt eliminating these diseases is the introduction of defective interfering particles (DIPs) (Huang and Baltimore, 1970; Rouzine and Weinberger, 2013). These DIPs are non-viable variants of the wild-type (WT) virus that lack essential elements needed for viral reproduction. They steal these elements from the WT virus in order to complete reproduction, thus interfering with the WT's ability to successfully spread.

1.2 Mathematical Modeling

With the numerous control measures at the hands of doctors and epidemiologists to use, it became important to find the most efficient and cost effective ways to implement those control measures. This is where mathematical modeling becomes a useful tool. The first disease control model was created by David Bernoulli in 1760 as a way to track how successful variolation, or inoculation of a small amount of smallpox, was in preventing the spread of smallpox (Anderson et al., 1992; Brauer et al., 2001).

Recently, multiscale models have become a popular tool. These models allow mathematicians to not only investigate host dynamics, but within-host dynamics as well. While models on the scale of human populations can capture how fast the disease is transitioning from one host to another, it can be beneficial to look at the pathogen level to gain an understanding of the biological workings of the disease. A combination of two scales would allow for greater biological accuracy. One example of this is tracking viral reproduction as well as the cells they infect. These models allow us to explore alternative control measures such as DIPs (Murillo et al., 2013; Rast et al., 2016; Rouzine and Weinberger, 2013; Thompson and Yin, 2010).

One of the simplest types of mathematical models to fight infectious diseases on any scale are compartmental models (Anderson et al., 1992; Brauer et al., 2001). These models group individuals (whether humans, animals, or even cells) based on certain characteristics such as those who are susceptible to a disease, those who are exposed, those who are infected, or those who have recovered. The movement from compartment to compartment can be reflected in differential equations. The simplest form of differential equation is ordinary differential equations. These use an exponential distribution for time spent in each compartment before moving on to the next. However, there are also models that implement delay differential equations or methods to incorporate various distributions for time spent in each compartment.

Another type of model that is commonly used, especially with the growth of computing power, is the agent-based stochastic model. This model allows mathematicians to look at individuals in a community, rather than grouping them into compartments, and make a decision based on social interactions (Gilbert, 2008; Murillo et al., 2013). The decision could be whether they will become infected based on coming into contact with an infected individual or move locations based on a current location or benefit of a new location. Agent-based models can be used on populations of any scale including humans, groups of individuals, bacteria, or even individual cells.

In this study, we look at various scales of infection and control such as quarantine for

Ebola at a human population scale, using social interactions to study the dynamics in biofilm formation at the cellular level, and using DIPs against poliovirus particles infecting cells and traveling between organs. These diseases or infections are difficult to control; there are either no vaccines, the vaccine is not enough to eliminate the disease, or they are becoming resistant to antibiotics. More specifically, in Chapter 2, we investigate how implementing control measures on certain population types can impact the type of distribution to use in a compartmental model. In Chapter 3, we use a stochastic spatial model to measure the benefit of a yeast strain expressing kin recognition when competing for resources against another strain in a biofilm. Finally, in Chapter 4, we use a two patch model to measure the dynamics of wild-type poliovirus and defective interfering particles as free virus particles spread between two organs.

Chapter 2

Applying Quarantine to Infectious: Does Ignoring Time Delay Lead to Incorrect Predictions? ¹

2.1 Introduction

Mathematical models have the potential to provide insight into the dynamics of an emerging disease. They can help determine the impact that control measures have before the epidemic becomes too severe (Anderson et al., 1992; Brauer et al., 2001). During the 2014 Ebola outbreak, a CDC modeling team immediately created two models (one with intervention and the other without) to determine how quickly control measures would slow the epidemic (Meltzer et al., 2014; Meltzer, 2016). This helped them estimate the amount of time they had to gather and send resources. When predicting the course of an epidemic, modelers must balance simplicity and accuracy. It is important to incorporate key characteristics of the disease, such as transmission and intervention methods. However, too many factors and complicated methods could make the system difficult and time consuming to

¹**Paper in preparation: Intervention Strategies for Epidemics: Does Ignoring Time Delay Lead to Incorrect Predictions? A. Bingham and L.B. Shaw.**

solve. For example, a complicated mathematical model that incorporates more parameters would require more data to estimate those parameters. If the parameter values are not fit to data correctly, it reduces the accuracy of the model predictions. Furthermore, if there is a rapidly spreading epidemic, such as Ebola, time is of the essence. In Meltzer (2016), it is stated that the turnaround time for answers to critical questions was less than one week. In addition, modelers must present their research to policy makers, and if the model is too complicated to communicate clearly, policy makers are less likely to accept the model and implement recommended controls in a timely manner, another problem CDC modelers faced during the 2014 outbreak (Meltzer et al., 2014; Meltzer, 2016).

One of the simpler methods to model an epidemic is using ordinary differential equations (ODEs) such as the SEIR compartmental model, where a population is divided into compartments of individuals who are susceptible (those able to become infected), exposed (those who are infected but cannot spread the disease), infectious (those who are able to spread the disease), or recovered (sometimes referred to as removed since they can no longer contract the disease) (Wearing et al., 2005; Li and Liu, 2014; Anderson et al., 1992; Kermack and McKendrick, 1927). Using ODEs involves assuming an exponential distribution for the time a person will spend in each compartment (Feng et al., 2007; Sherborne et al., 2015; Li and Liu, 2014; Yang et al., 2008; Huang et al., 2010; Zhang et al., 2009). However, ODEs can lead to underestimates of the infectious steady state due to the exponential distribution's large variance (Wearing et al., 2005; Yang et al., 2008; Feng et al., 2007; Sherborne et al., 2015). This occurs because a large variance can allow for a higher probability of an unrealistically short time spent, for example, exposed or infectious.

We would like to use a distribution with a much smaller variance for the time remaining in each compartment. For instance, the gamma and Poisson distributions have been used to model the exposed and infectious periods of various diseases such as smallpox, anthrax, and influenza due to the reduced size in variance of the distributions (Brookmeyer et al., 2005; Eichner and Dietz, 2003; Nishiura, 2007). This allows for more realistic times spent exposed or infectious. We focus on the delta distribution, which has constant exposed and

infectious periods and a variance of zero. With this lack of variance, we limit the parameters we need to estimate. This type of distribution can be represented using delay differential equations (DDEs) (Huang et al., 2010; Keeling and Grenfell, 2002). However, it is more difficult to numerically evaluate DDEs than it is to evaluate ODEs because DDEs depend on a history of solutions to calculate the next time step. Also, most epidemic models are stiff systems due to processes occurring on multiple time scales (Shampine and Thompson, 2001). For instance, a model could include the average lifetime of an individual, which could span years, while also including the time span of a disease in days. Solving stiff systems becomes more difficult when time delays are involved. Therefore, it is our goal to highlight certain cases when it is best to use delay differential equations versus when the simpler ordinary differential equations can be used.

In this study, we will compare an exponential model, which uses ordinary differential equations, and a delay differential equation model, with time delays in both an exposed and an infectious class, using a model with multiple exposed and infectious compartments to interpolate between the two. All three models will include quarantine of the infectious class as the main control measure. Section 2.2 introduces the models, and Section 2.3 reports the steady states and basic reproduction numbers. In Section 2.4, we compare the effect of control in the exponential and delay models where we have used simulated data to fit the transmission rate for each model. As expected, we see an underestimation in the infectious steady state of the exponential system when applying a quarantine measure. Next, in Section 2.5, we explore whether the time delay in the exposed class or the time delay in the infectious class has the greatest impact on the infectious steady state. Then, in Section 2.6, we explore how the length of each time delay affects the difference between the exponential and the delay systems' infectious steady states. Finally, in Section 2.7, we compare our quarantine results with two other possible control measures, isolation of exposed individuals and vaccination of susceptibles.

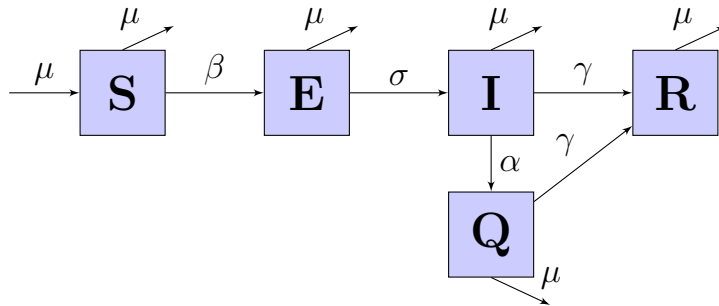


Figure 2.1 Flow chart for SEIQR model, where μ is the population birth and death rate, β is the infection rate, σ is the incubation rate, α is the quarantine rate, and γ is the recovery rate

2.2 Models

For this project we will use Ebola parameters from Hu et al. (2015). At the time of the 2014 outbreak, Ebola was spreading rapidly, so it was important that accurate models were produced quickly. Additionally, there were numerous intervention methods applied, including quarantine, hospitalization rates, and safe burial practices (Haas, 2014; Pandey et al., 2014; Meltzer et al., 2014; Meltzer, 2016). Finally, because the incubation period and infectious period for Ebola are relatively long compared to diseases such as influenza and measles (Hethcote, 2000; Wearing et al., 2005; Safi and Gumel, 2011), we suspected the distributions of these periods could be especially important, although that will be explored in detail in Section 2.6 .

In the following three models, we will focus on the intervention method of quarantine. A quarantine rate is applied to the infectious population, where a proportion of the infectious population will be isolated and unable to spread the disease. They will eventually enter the recovered class (see Fig. 2.1). Later, in Section 2.7, we will investigate what happens when control is applied to the exposed or susceptible classes.

| Parameter | Definition | Value |
|-----------|---|---|
| μ | Birth and death rate | 0.00005 days ⁻¹ |
| β | Transmission rate | 0.278 days ⁻¹ |
| σ | Incubation rate | 0.10 days ⁻¹ |
| γ | Recovery rate | 0.18 days ⁻¹ |
| α | Quarantine rate | 0.05 days ⁻¹ (Meltzer, 2016) |
| τ_1 | Incubation delay ($\frac{1}{\sigma}$) | 10 days |
| τ_2 | Recovery delay ($\frac{1}{\gamma}$) | 50/9 days |
| n | Number of exposed compartments | 1 to ∞ |
| m | Number of infectious compartments | 1 to ∞ |

Table 2.1 Model parameters (derived from Hu et al. (2015) except where indicated)

We first introduce the exponential version of the SEIR model with a quarantined class:

$$\begin{cases} \frac{dS}{dt} = \mu - \beta SI - \mu S \\ \frac{dE}{dt} = \beta SI - (\mu + \sigma)E \\ \frac{dI}{dt} = \sigma E - (\mu + \alpha + \gamma)I \\ \frac{dQ}{dt} = \alpha I - (\mu + \gamma)Q \\ \frac{dR}{dt} = \gamma(I + Q) - \mu R \end{cases} \quad (2.1)$$

where S is the proportion of susceptibles in the population, E is the proportion of exposed, I is the proportion of infectious, Q is the proportion in quarantine, and R is the proportion of removed individuals at time t . We have a transmission rate β , incubation rate σ to advance from exposed to infectious, quarantine rate α , recovery rate γ , and birth and death rate μ . All rates are per day (see Table 2.1). For the quarantine rate, we use $\alpha = 0.05$. According to Meltzer (2016) and Washington and Meltzer (2015), about 20% of Ebola patients were put into Ebola treatment units between September and October of 2014. While other papers reference a higher quarantine rate for best case scenarios (Hu et al., 2015; Hethcote et al., 2002), we want to focus on a smaller α since our goal is not to guarantee epidemic extinction but rather to study the influence of control measures on accuracy in model predictions.

Our delay differential equation model includes time delays τ_1 and τ_2 , where τ_1 represents

the time spent in the exposed compartment and τ_2 represents the time spent in the infectious compartment:

$$\left\{ \begin{array}{l} \frac{dS}{dt} = \mu - \beta SI - \mu S \\ \frac{dE}{dt} = \beta SI - \beta S(t - \tau_1)I(t - \tau_1)e^{-\mu\tau_1} - \mu E \\ \frac{dI}{dt} = \beta S(t - \tau_1)I(t - \tau_1)e^{-\mu\tau_1} \\ \quad - \beta S(t - \tau_1 - \tau_2)I(t - \tau_1 - \tau_2)e^{-\mu(\tau_1 + \tau_2) - \alpha\tau_2} - (\mu + \alpha)I \\ \frac{dQ}{dt} = \alpha I - \mu Q - \beta S(t - \tau_1 - \tau_2)I(t - \tau_1 - \tau_2)e^{-\mu(\tau_1 + \tau_2)}(1 - e^{-\alpha\tau_2}) \\ \frac{dR}{dt} = \beta S(t - \tau_1 - \tau_2)I(t - \tau_1 - \tau_2)e^{-\mu(\tau_1 + \tau_2)} - \mu R \end{array} \right. . \quad (2.2)$$

The rate of entry into the infectious class from the exposed class at time t is $\beta S(t - \tau_1)I(t - \tau_1)e^{-\mu\tau_1}$, where a person who becomes infectious at t was exposed at time $t - \tau_1$ and remained exposed for length of time τ_1 (Cooke et al., 1999). The factor $e^{-\mu\tau_1}$ is the probability an exposed individual will survive to reach the infectious class (Beretta and Breda, 2011; Kaddar et al., 2011; Li and Liu, 2014). Similarly, entry into the recovered class from the infectious class occurs at rate

$$\beta S(t - \tau_1 - \tau_2)I(t - \tau_1 - \tau_2)e^{-\mu(\tau_1 + \tau_2)}e^{-\alpha\tau_2},$$

where a person recovering at time t was exposed at time $t - \tau_1 - \tau_2$, and the probability the person survives to reach the recovered class is $e^{-\mu(\tau_1 + \tau_2)}$. The probability a person does not become quarantined and moves straight from infectious to the recovered class is $e^{-\alpha\tau_2}$. In the equation for Q , $1 - e^{-\alpha\tau_2}$ represents the probability an individual did become quarantined.

Note that although it is possible to exclude $\frac{dE}{dt}$ and $\frac{dR}{dt}$ because they do not affect the other compartments, we include these equations for completeness and to emphasize the fact that we have a closed system. In other words, our total population is always 100%.

To be able to compare the delay model to the exponential model, the time delays must correspond to the average times in each compartment in the exponential model. The transition rate from the exposed compartment to the infectious compartment is σ , so the

average time spent in the exposed class is $\frac{1}{\sigma}$. This is our τ_1 . Similarly, $\tau_2 = \frac{1}{\gamma}$.

Our third model, the multi-infected compartment model, breaks the disease classes of the exponential model into n number of exposed compartments, m number of infectious compartments, and m number of quarantine compartments. This method is similar to the method used in Wearing et al. (2005). However, their model focused on contact tracing and divided the infectious individuals into asymptomatic and symptomatic categories while putting individuals who were exposed, whether they obtained the disease or not, into quarantine. In our model, the number of infectious and quarantine compartments will always be equal (see Fig. 2.2) since recovery in the infectious class will take just as long in the quarantine class:

$$\left\{ \begin{array}{l} \frac{dS}{dt} = \mu - \beta S \left(\sum_{i=1}^m I_i \right) - \mu S \\ \frac{dE_1}{dt} = \beta S \left(\sum_{i=1}^m I_i \right) - \mu E_1 - n\sigma E_1 \\ \vdots \\ \frac{dE_n}{dt} = n\sigma E_{n-1} - \mu E_n - n\sigma E_n \\ \frac{dI_1}{dt} = n\sigma E_n - \mu I_1 - (\alpha + m\gamma)I_1 \\ \vdots \\ \frac{dI_m}{dt} = m\gamma I_{m-1} - (\mu + \alpha + m\gamma)I_m \\ \frac{dQ_1}{dt} = \alpha I_1 - (\mu + \gamma m)Q_1 \\ \vdots \\ \frac{dQ_m}{dt} = \alpha I_m + \gamma m Q_{m-1} - (\mu + \gamma m)Q_m \\ \frac{dR}{dt} = \gamma m (I_m + Q_m) - \mu R \end{array} \right. \quad (2.3)$$

The term $\sum_{i=1}^m I_i$ represents the total number of infectious individuals in the population at time t . Again, we need to make sure the average time spent in each class is equivalent to the other models. If there are n compartments in the exposed class and the average time to become infectious is $\frac{1}{\sigma}$, then the average time in each exposed compartment is $\frac{1}{n\sigma}$, making

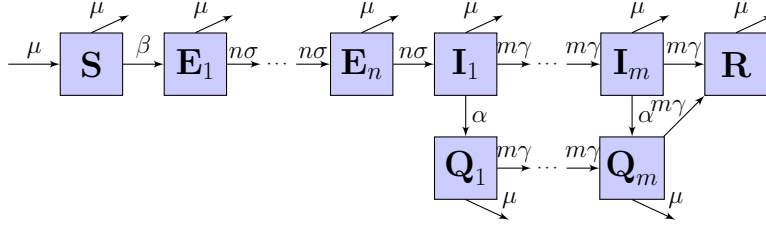


Figure 2.2 Flow chart for multi-infected compartment model, where n is the number of exposed compartments and m is the number of infectious/quarantine compartments.

the rate to progress out of each compartment $n\sigma$. Similarly, the rate to progress from each infectious compartment is $m\gamma$.

This model uses a gamma distribution for time spent exposed and infectious, with the number of compartments affecting the shape of the distribution. As n and m increase towards infinity, the model approaches a delta distribution for time spent exposed and infectious, allowing us to observe the effect of constant exposed and infectious periods (see Fig. 2.3) (Sherborne et al., 2015; Leemis, 2011; Cox and Miller, 1965; Feng et al., 2007). When $n = m = 1$, the model uses an exponential distribution for time spent exposed and infectious, equivalent to Eq. (2.1). Therefore, we will use this model to gradually change from the exponential model to the delay model and investigate which delays are causing the greatest change in dynamics.

2.3 Steady States and Basic Reproduction Numbers

As mentioned before, some models that include multiple time spans can be stiff. While there are solvers made to adjust the time steps with respect to the time delays (Shampine and Thompson, 2001), our system proved to be too stiff for numerically accurate simulations. Our system also includes a combination of multiple time delays, increasing the difficulty in obtaining numerics. We focus primarily on analytics and find the endemic steady state of each model, with emphasis on the number of infectious individuals. We then calculate the basic reproduction number for each model.

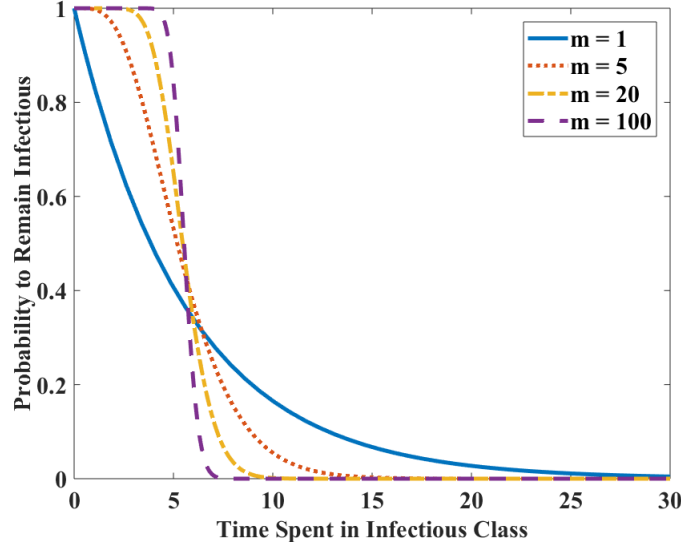


Figure 2.3 Interpolation between the exponential and the delay model by the multi-infected compartment model. When m , the number of infectious compartments, is 1, the model assumes an exponential distribution. As m increases, the model approaches a constant infectious period, which is used by the delay model

2.3.1 Exponential Model

The exponential system yields a disease free state of $(S_E^0, E_E^0, I_E^0, Q_E^0, R_E^0) = (1, 0, 0, 0, 0)$. There is also an endemic steady state $(S_E^*, E_E^*, I_E^*, Q_E^*, R_E^*)$, where our main focus will be on the infectious steady state (see Appendix 2.9.1 for full steady state),

$$I_E^* = \frac{\mu}{\alpha + \mu} \left(\frac{\sigma}{\sigma + \mu} \right) \left[1 - \left(\frac{\gamma}{\gamma + \alpha + \mu} \right) \right] - \frac{\mu}{\beta}. \quad (2.4)$$

We can find the basic reproduction number using the method outlined by Van den Driessche and Watmough (2002), obtaining

$$R_0 = \frac{\beta\sigma}{(\sigma + \mu)(\alpha + \gamma + \mu)}.$$

For the Ebola parameters listed in Table 2.1, $R_0 > 1$. This implies that the disease free state is unstable under these parameters. By numerically calculating the Jacobian at the endemic equilibrium and its eigenvalues, it can be shown that the endemic steady state is

stable under these parameters.

2.3.2 Delay Differential Equation Model

The disease free steady state of the delay differential equation model is identical to the exponential system, and the endemic steady state (see Appendix 2.9.2 for the full steady state) includes the infectious steady state

$$I_D^* = \frac{\mu}{\alpha + \mu} e^{-\mu\tau_1} [1 - e^{-(\mu+\alpha)\tau_2}] - \frac{\mu}{\beta}. \quad (2.5)$$

In order to find the basic reproduction number, we take the limit of the basic reproduction number of the multi-infected compartment model (see next subsection) as n and m approach infinity (Wearing et al., 2005). Also, recall that $\tau_1 = 1/\sigma$ and $\tau_2 = 1/\gamma$. This results in

$$R_0 = \frac{\beta}{\mu + \alpha} [e^{-\mu\tau_1}] [1 - e^{-(\mu+\alpha)\tau_2}]. \quad (2.6)$$

2.3.3 Multi-Infected Compartment Model

The disease free steady state of the multi-infected compartment model is similar to the previous two models: $(S_M^0, E_{M,1}^0, E_{M,2}^0, \dots, E_{M,n}^0, I_{M,1}^0, I_{M,2}^0, \dots, I_{M,m}^0, Q_{M,1}^0, Q_{M,2}^0, \dots, Q_{M,m}^0, R_M^0) = (1, 0, 0, \dots, 0, 0, 0, \dots, 0, 0, 0, \dots, 0, 0)$.

We now outline how we find the endemic steady state. Our main focus will be on the sum of all infectious compartments at steady state, $\sum_{i=1}^m I_{M,i}^*$, so we will express other quantities in terms of that sum. First, we note that at steady state,

$$S_M^* = \frac{\mu}{\beta \sum_{i=1}^m I_{M,i}^* + \mu}$$

and

$$E_{M,1}^* = \frac{\beta \mu \sum_{i=1}^m I_{M,i}^*}{(\mu + n\sigma)(\beta \sum_{i=1}^m I_{M,i}^* + \mu)}. \quad (2.7)$$

Now, we find the steady state relationships between exposed classes $E_{M,1}^*, E_{M,2}^*,$

... $E_{M,n}^*$, where

$$E_{M,i}^* = \left(\frac{n\sigma}{\mu + n\sigma} \right)^{i-1} E_{M,1}^*$$

for $i \in \{2, \dots, n\}$, indicating that

$$\sum_{i=1}^n E_{M,i}^* = E_{M,1}^* \sum_{j=0}^{n-1} \left(\frac{n\sigma}{\mu + n\sigma} \right)^j.$$

This a finite geometric series, and after substituting $E_{M,1}^*$ with (2.7), we find that

$$\sum_{i=1}^n E_{M,i}^* = \frac{\beta \sum_{i=1}^m I_{M,i}^* \left[1 - \left(\frac{n\sigma}{n\sigma + \mu} \right)^n \right]}{\beta \sum_{i=1}^m I_{M,i}^* + \mu}.$$

We now consider the steady state for the quarantined and recovered population $\sum_{i=1}^m Q_i + R$. In general,

$$\frac{d}{dt} \left[\sum_{i=1}^m Q_i + R \right] = \alpha \sum_{i=1}^m I_i - \mu \sum_{i=1}^m Q_i - \mu R + m\gamma I_m.$$

At steady state

$$I_{M,i}^* = \left(\frac{m\gamma}{\mu + \alpha + m\gamma} \right)^{i-1} I_{M,1}^*$$

for $i \in \{2, \dots, n\}$ and where

$$I_{M,1}^* = \frac{n\sigma E_{M,n}^*}{\mu + \alpha + m\gamma}.$$

Therefore,

$$\left(\sum_{i=1}^m Q_i + R \right)_M^* = \frac{\alpha}{\mu} \sum_{i=1}^m I_{M,i}^* + \left(\frac{m\gamma}{\mu + \alpha + m\gamma} \right)^m \left(\frac{n\sigma}{\mu + n\sigma} \right)^n \left(\frac{\beta \sum_{i=1}^m I_{M,i}^*}{\beta \sum_{i=1}^m I_{M,i}^* + \mu} \right).$$

Finally, using the property of a closed system, $S_M^* + \sum_{i=1}^n E_{M,i}^* + \sum_{i=1}^m I_{M,i}^* + (\sum_{i=1}^m Q_i + R)_M^* = 1$, we solve for $\sum_{i=1}^m I_{M,i}^*$:

$$\sum_{i=1}^m I_{M,i}^* = \frac{\mu}{\alpha + \mu} C_E C_I - \frac{\mu}{\beta}, \quad (2.8)$$

where we define constants

$$C_E = \left(\frac{n\sigma}{n\sigma + \mu} \right)^n \quad (2.9)$$

and

$$C_I = 1 - \left(\frac{m\gamma}{m\gamma + \alpha + \mu} \right)^m. \quad (2.10)$$

Again using the method from Van den Driessche and Watmough (2002) (see Appendix 2.9.3 for details), the R_0 value is found to be

$$R_0 = \frac{\beta}{\mu + \alpha} C_E C_I. \quad (2.11)$$

2.4 Example of Underestimation of Infectious Population in Exponential System

When modeling a new epidemic, one of the more complicated parameters to estimate is the transmission rate (Hu et al., 2015; Hethcote, 2000). It is easier to estimate from data how many people are infected, how many people are being quarantined, or how many people have recovered. It is not as simple to calculate how often infectious people come into contact with susceptible people, and even more complicated to determine if the disease was transmitted with that contact. To mirror the process of estimating the transmission rate of a real disease using a simple model before applying a control, we will fit our transmission rate β in the exponential model to simulated data coming from the infectious steady state of the delay system. We will then investigate whether applying a control leads to an underestimation in the infectious steady state of the exponential system like that observed by Wearing et al. (2005).

The procedure is shown in Fig. 2.4a. We first begin by matching the infectious steady states of the exponential system (2.4) and the delay system (2.5) without any control ($\alpha = 0$). We will take our exponential system to be the “predicted” or “simple” system and the delay system to be our “real” system. This is because the delay system is likely more accurate with

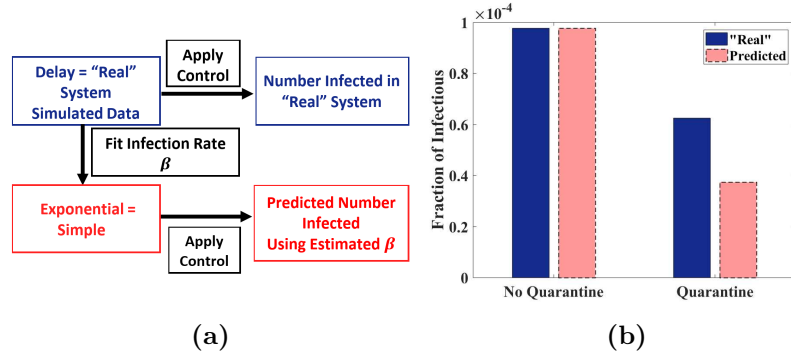


Figure 2.4 (a) Schematic for fitting β and applying control to measure underestimation in exponential system. (b) Numerical results for fitting β , applying quarantine control, and comparing the “real” delay system and the “predicted” exponential system

its delta distribution and correspondingly small variance in exposed and infectious periods.

Therefore, if $I_E^* = I_D^*$, then

$$\frac{\mu}{\alpha + \mu} \left(\frac{\sigma}{\sigma + \mu} \right) \left[1 - \left(\frac{\gamma}{\gamma + \alpha + \mu} \right) \right] - \frac{\mu}{\beta_{\text{est}}} = \frac{\mu}{\alpha + \mu} e^{-\mu\tau_1} [1 - e^{-(\mu+\alpha)\tau_2}] - \frac{\mu}{\beta_{\text{real}}},$$

where β_{real} is the transmission rate in the delay system and β_{est} is the estimated transmission rate that allows the exponential system to match the delay system. Solving, we find

$$\beta_{\text{est}} = \frac{(\mu + \sigma)(\gamma + \mu)\beta_{\text{real}}\mu}{(\sigma + u)(\gamma + \mu)(\beta_{\text{real}}e^{-(\mu(\tau_1+\tau_2))} - \beta_{\text{real}}e^{-\mu\tau_1} + \mu) + \sigma\beta_{\text{real}}\mu}. \quad (2.12)$$

We then substitute this estimated β in for the transmission rate of our exponential steady state, (2.4), with $\alpha \neq 0$:

$$I_{\text{est}}^* = \frac{-\mu\sigma\alpha}{(\mu + \sigma)(\gamma + \mu)(\alpha + \gamma + \mu)} + e^{-\mu\tau_1}(1 - e^{-\mu\tau_2}) - \frac{\mu}{\beta_{\text{real}}} \quad (2.13)$$

If we substitute our parameter values from Table 1 into (2.5) and (2.13) and observe the numerical results in Fig. 2.4b, we can see that the “predicted” number of infectious people is about half the “real” number of infectious people.

To determine if we see underestimation in a more general scenario, we compare (2.13) analytically to our delay steady state, (2.5), also with $\alpha \neq 0$. For simplicity, we Taylor expand to find the leading order term in μ , assuming that $\mu \ll \alpha, \gamma, \sigma$ since $\frac{1}{\mu}$ represents the length of a lifetime in days and is much longer than the length of quarantine, infectious, and exposed periods.

This leads to $I_D^* \approx \frac{\mu}{\alpha} (1 - e^{-\alpha/\gamma}) - \frac{\mu}{\beta_{\text{real}}}$ and $I_{\text{est}}^* \approx \frac{\mu}{\gamma} \left(1 - \frac{\alpha}{\alpha + \gamma}\right) - \frac{\mu}{\beta_{\text{real}}}$. Thus comparing the “real” and “predicted” infection levels requires comparing factor $C_D = 1 - e^{-\alpha/\gamma}$ to factor $C_{\text{est}} = \frac{\alpha}{\gamma} \left(1 - \frac{\alpha}{\alpha + \gamma}\right)$.

At this point, it is still difficult to tell which is greater, but we can conclude that the extent of the discrepancy between the “real” system and the “predicted” system depends on the quarantine rate and the recovery rate.

If we further assume a small quarantine rate such that $\alpha \ll \gamma$, we can expand the two steady states further and find that $C_D \approx \frac{\alpha}{\gamma} \left(1 - \frac{\alpha}{2\gamma}\right)$ and $C_{\text{est}} \approx \frac{\alpha}{\gamma} \left(1 - \frac{\alpha}{\gamma}\right)$. In this limit, $C_D > C_{\text{est}}$.

Therefore, at least for low quarantine, it can be seen that the “predicted” exponential system’s infectious steady state is less than the “real” delay system’s infectious steady state, confirming that the exponential system will underestimate the number of infectious in our model when a control measure is applied.

2.5 Effect of Number of Compartments on Infectious Steady State

We can use the multi-infected compartment model to interpolate between the exponential system and the delay system by varying the number of compartments. Now we want to investigate how this variation will affect the infectious steady state. It is important to know if a particular method of modeling tends to overestimate or underestimate the infectious steady state when attempting to apply accurate control measures. We begin by taking (2.8) and letting the number of exposed compartments, n , increase to infinity while maintaining

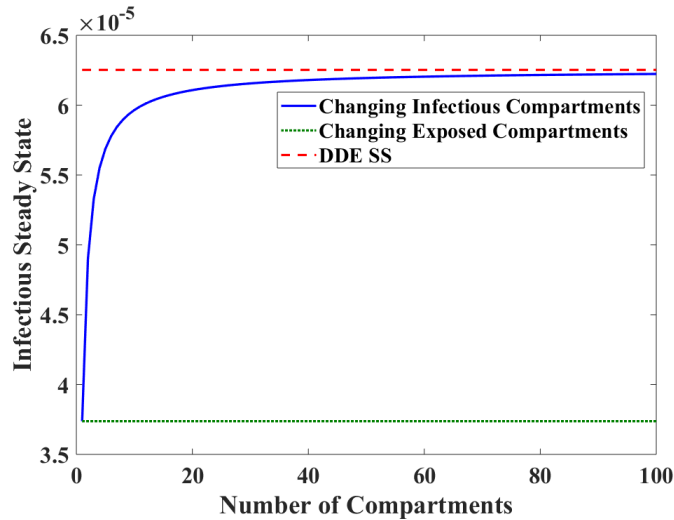


Figure 2.5 Infectious steady state of the multi-infected model as the number of exposed (dotted curve) or infectious (solid curve) compartments increases. The infectious steady state of the delay system is shown for comparison (dashed curve)

only one infectious compartment and one quarantine compartment, $m = 1$. This allows the distribution of the exposed period to move from an exponential distribution to a constant period while the infectious period remains exponentially distributed. We will be able to see if the narrower distribution of the exposed class increases or decreases the infectious steady state, impacting the needed amount of control. We then repeat this analysis for the infectious class, allowing the number of infectious compartments, m , to increase to infinity while maintaining only one exposed compartment.

In Fig. 2.5, using parameters from Table 2.1, we can see that as the number of infectious compartments increases, the multi-infected system's infectious steady state approaches the delay system's steady state. However, as the number of exposed compartments increases, the multi-infected system's infectious steady state seems to stay constant.

We now analytically investigate this result in order to form a more general argument beginning with the change in the number of exposed compartments. Since we are only changing n , we focus on C_E (2.9), which when increased, increases the infectious steady state.

When $n = 1$, the exposed class has an exponential distribution and C_E becomes

$$\frac{1}{\frac{\mu}{\sigma} + 1}. \quad (2.14)$$

As n approaches infinity, the distribution of time spent exposed approaches a delta distribution and C_E becomes

$$e^{-\mu/\sigma}. \quad (2.15)$$

Next, we assume that $\frac{\mu}{\sigma} \ll 1$ due to the much smaller birth rate. We use a Taylor expansion to the second order on (2.14) about $\frac{\mu}{\sigma}$, resulting in

$$1 - \frac{\mu}{\sigma} + \left(\frac{\mu}{\sigma}\right)^2. \quad (2.16)$$

The Taylor expansion for (2.15) about $\frac{\mu}{\sigma}$ results in

$$1 - \frac{\mu}{\sigma} + \left(\frac{1}{2}\right) \left(\frac{\mu}{\sigma}\right)^2. \quad (2.17)$$

Comparing the two expanded terms, we see that C_E using an exponential distribution is greater than C_E using a delay distribution, or

$$\frac{1}{\frac{\mu}{\sigma} + 1} > e^{-\mu/\sigma}.$$

Therefore, using DDEs (or a delta distribution) for the exposed class will decrease the infectious steady state. However, comparing this to our numerical results in Fig. 2.5, we observe a negligible decrease in the infectious steady state.

Next, we perform the same analysis for varying the number of infectious compartments, m . This time, we focus on C_I (2.10), which when increased, also increases the infectious steady state.

Again, we can assume $\frac{\mu}{\gamma} \ll 1$ due to difference in time scales. For convenience, we make an extra, potentially unrealistic, assumption that the quarantine rate α is much smaller than

the recovery rate γ . Letting $m = 1$ gives us an exponential distribution in the infectious compartment and C_I becomes

$$1 - \left(\frac{1}{1 + \frac{\mu + \alpha}{\gamma}} \right) \quad (2.18)$$

with a Taylor expansion to the second order about small $\frac{\mu + \alpha}{\gamma}$ of

$$\frac{\mu + \alpha}{\gamma} - \left(\frac{\mu + \alpha}{\gamma} \right)^2. \quad (2.19)$$

As m approaches infinity, the infectious class approaches a delta distribution and C_I becomes

$$1 - e^{-(\mu + \alpha)/\gamma} \quad (2.20)$$

with a Taylor expansion to the second order about small $\frac{\mu + \alpha}{\gamma}$ of

$$\frac{\mu + \alpha}{\gamma} - \left(\frac{1}{2} \right) \left(\frac{\mu + \alpha}{\gamma} \right)^2. \quad (2.21)$$

Comparing the two expanded terms, we see that C_I using a delta distribution is greater than C_I using an exponential distribution, or

$$1 - \frac{\gamma}{\alpha + \gamma + \mu} < 1 - e^{-(\mu + \alpha)/\gamma}.$$

Thus, using DDEs for the infectious class will increase the infectious steady state.

Numerically, we have shown that increasing the number of infectious compartments allows the infectious steady state to reach more accurate levels, while increasing the number of exposed compartments has little impact. When investigating this analytically, using a time delay in the exposed compartment appears to decrease the infectious steady state. For small control levels, we showed analytically that using a time delay in the infectious compartment increases the infectious steady state.

Together, these results reinforce that using an exponential distribution can lead to underestimate in predicted steady states, with new emphasis on using the correct distribution

in the infectious class.

2.6 Effect of Length of Time Delay on Infectious Steady State

We now investigate whether the length of the time delay has an impact on the discrepancy between the exponential and the delay systems' infectious steady states. We test this by focusing on each time delay separately.

We first look at the time delay in the exposed class, varying τ_1 while assuming the infectious period and number of infectious compartments are fixed. Therefore, we again only need to focus on C_E (2.9). To study the difference between the steady state of the exponential and delay system, we need to use the expanded form of (2.14) and (2.15) for slow birth rate. Subtracting (2.17) from (2.16) results in

$$\left(\frac{1}{2}\right) \left(\frac{\mu}{\sigma}\right)^2.$$

Thus the exponential system's infectious steady exceeds that of the delay system by

$$\frac{\mu}{\alpha + \mu} C_I \frac{1}{2} (\mu\tau_1)^2 \tag{2.22}$$

since $\tau_1 = \frac{1}{\sigma}$. (Recall that C_I is independent of σ and τ_1 .) As the time delay in the exposed class increases, the discrepancy between the infectious steady state of the exponential and the delay system increases.

In Fig. 2.6a we plot the percent difference in the infectious steady state between using an exponential distribution and delay distribution in the exposed class as τ_1 increases. We maintain a time delay in the infectious compartment for consistency. We see that the percent difference is quite small, implying that the time delay in the exposed class has little impact on the difference in infectious steady states.

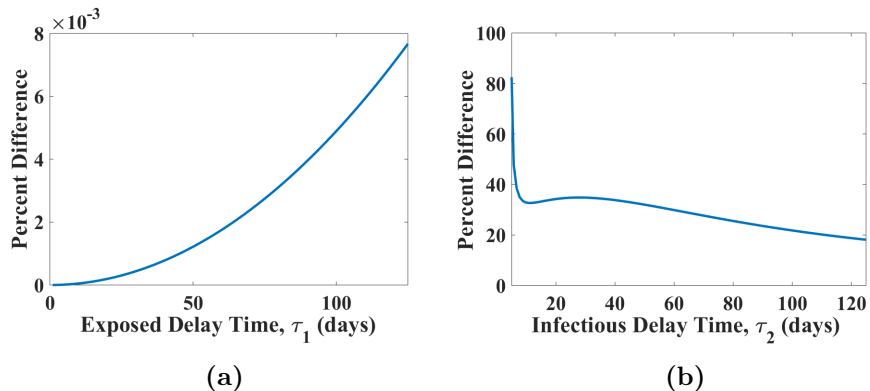


Figure 2.6 (a) Percent difference in infectious steady state between using an exponential distribution and delay distribution in the exposed class versus time spent exposed, τ_1 . (b) Percent difference between using an exponential distribution and delay distribution in the infectious class versus time spent infectious, τ_2

Note that in Fig. 2.6a we stop τ_1 at 123 days because of the existence of a Hopf bifurcation in the delay system at approximately $\tau_1 = 123.75$, after which the infectious steady state is less relevant. In order to locate the Hopf bifurcation, we tested different values for τ_1 and used `dde23` in Matlab to numerically integrate (2.2) from an initial condition that included a slight perturbation from the endemic steady state. For $\tau_1 < 123.5$, the system approached the endemic steady state. For $\tau_1 > 123.75$, the system continued to oscillate with increasing amplitude.

A similar approach to finding the discrepancy between the two steady states by varying the delay τ_2 in the infectious compartment would require us to focus on C_I (2.10). However, we cannot make simplifying assumptions in a convenient limit because if τ_2 is long, the assumption that the quarantine rate, α , is slow compared to the recovery rate γ (made in the expansion of C_I in (2.19) and (2.21)) does not hold, while if the infectious period τ_2 is too short, the system will approach the disease free state.

Therefore, we resort to numerics. The percent difference between using an exponential distribution and delay distribution for the infectious class is plotted in Fig 2.6b. Again, a time delay was used in the exposed class for consistency. This time, we see that the delay in the infectious class has a much greater impact on the difference between the infectious

steady states and that smaller time delays contribute to greater differences.

Note that by numerically searching for a Hopf bifurcation, we determined that there was no Hopf bifurcation for $\tau_2 < 125$. However, the system appears to be below epidemic threshold at $\tau_2 = 4.25$ days, so we only plot for $\tau_2 \geq 5$ days.

2.7 Effects of Different Control Applications

We next consider other control strategies that are applied to different subsets of the population and whether that has an impact on if time delays must be used. For instance, would applying a vaccine to the susceptible population lead to different results than applying quarantine to an exposed population when time delays were used?

We first investigate the case where there was no control. For our analysis, we use our models with $\alpha = 0$ and parameters from Table 2.1. As we already saw with infectious quarantine control, the exponential model underestimates the infectious steady state as compared with the delay model. As we increase the number of exposed and infectious compartments, the multi-infected infectious steady state (see (2.8) for $\alpha = 0$) increases to approach the delay system's infectious steady state (see Fig. 2.7a). Similar to the case where quarantine was applied to the infectious class, the number of exposed compartments has little impact on changing the multi-infected system's infectious steady state, while increasing the number of infectious compartments helps increase the multi-infected infectious steady state to match the delay system (data not shown).

We observe a similar scenario when applying a vaccine to the susceptible class. In this model, a proportion of the susceptible population is transferred at vaccination rate ν to the recovered/removed class (see Fig. 2.8). Steady states are given in Appendix 2.9.4. Again, the exponential model underestimates the infectious steady state (data not shown). As we increase the number of infectious compartments, the multi-infected infectious steady state also increases to approach the delay steady state. Increasing the number of exposed compartments has little effect on the infectious steady state.

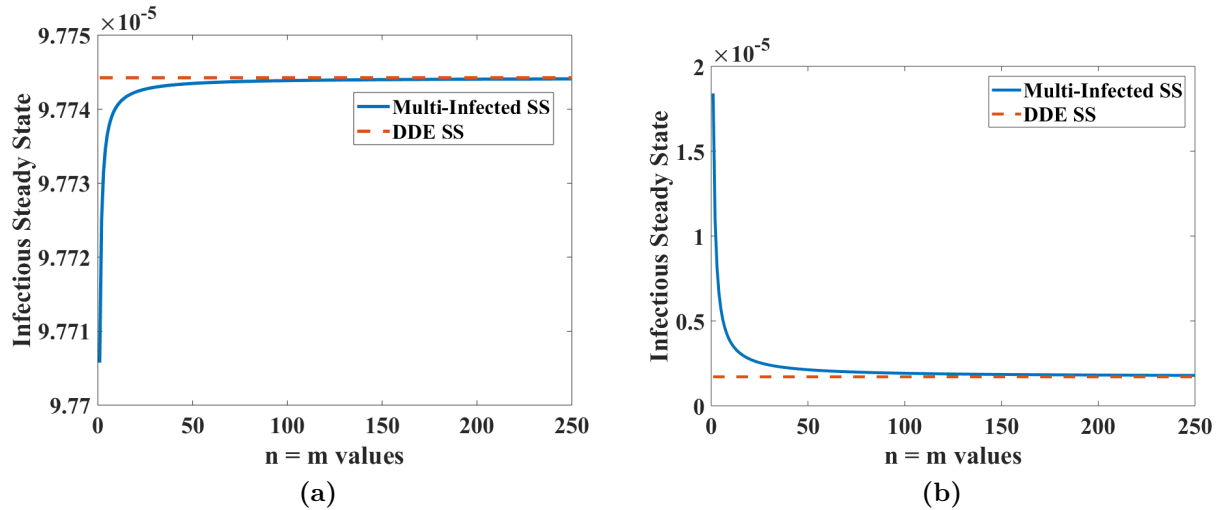


Figure 2.7 (a) Infectious steady state of a system without any control measure as the number of infectious compartments, m , and the number of exposed compartments, n increases at the same rate. (b) Infectious steady state when quarantine is applied to the exposed class as the number of infectious compartments, m , and the number of exposed compartments, n increases at the same rate. The same quarantine rate is used on the exposed class as was used on the infectious class. See Table 2.1

Lastly, we investigate what happens when we apply quarantine to the exposed class rather than to the infectious class. Individuals are still quarantined at rate α and progress through the n quarantine compartments (see Fig. 2.9). Assuming they are being cured while in the quarantine class, they move straight into the recovered class after n quarantine compartments. The infectious steady state is given in Appendix 2.9.5. In contrast to the other control strategies we considered, quarantine of exposed individuals can lead to the exponential system overestimating the infectious steady state as compared with the delay system. For the parameters studied, the multi-infected compartment's infectious steady state actually decreases to approach a smaller delay system infectious steady state (see Fig. 2.7b). Also, the number of exposed compartments contributes mostly to the decrease in infectious steady state where the number of infectious compartments has little impact on the change in infectious steady state. This implies that a time delay would be more beneficial in the exposed class rather than the infectious class as seen when applying a quarantine to the infectious class.

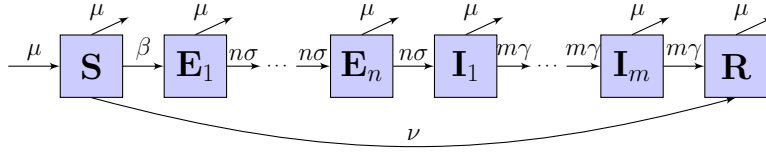


Figure 2.8 Flow chart for multi-infected compartment model with a vaccine applied to the susceptible class, where n is the number of exposed compartments, m is the number of infectious compartments, and ν is the vaccination rate. Other parameters are as before. See Table 2.1

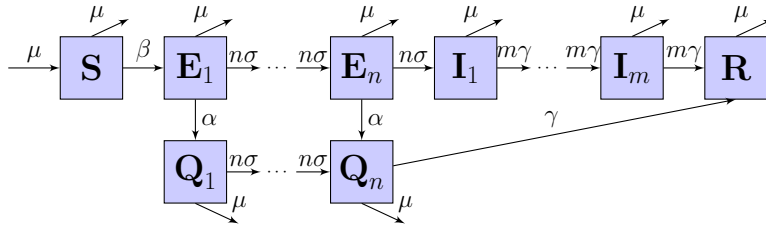


Figure 2.9 Flow chart for multi-infected compartment model with a quarantine applied to the exposed class, where n is the number of exposed/quarantine compartments and m is the number of infectious compartments. Other parameters are as before. See Table 2.1

In a similar observation made by Wearing et al. (2005), adding more compartments the exposed class slows down the movement of exposed individuals who would otherwise quickly move into the infectious class. This allows for more of them to become quarantined and results in fewer of them spreading the disease. When quarantine was applied to the infectious class, there were still individuals spreading the disease before having a chance to become quarantined. Adding more compartments slows down the movement of infectious individuals into the recovered class, allowing for more disease spread and, therefore, increasing the infectious steady state.

2.8 Conclusion

Mathematical models play an important role in predicting the size of an infectious population during an epidemic outbreak. The size of the infectious population is key for allocating resources, time, and money. As explained by Meltzer (2016), some mathematical

models need to be produced and evaluated under a strict time constraint. Therefore it can be preferable to use the quickest and easiest method even if it sacrifices some accuracy. The exponential system is favorable due to its ease, but if mathematicians are not careful, the parameters used could lead to a significant underestimation of the infectious steady state as highlighted in Wearing et al. (2005). We also observed an underestimation of the infectious steady state of our exponential model when fitting the transmission rate and applying quarantine of infectious individuals. This underestimation could lead to inaccuracies in the amount of control recommended, which could lead to difficulty in eradicating the epidemic.

To explore in more detail the role of the distribution used for the time spent exposed or infectious, we created a multi-infected compartment model to interpolate between our exponential model and our delay model and explored whether a particular time delay had a greater impact on the infectious steady state, which could help to make an epidemic model more simple and accurate. We found that using a time delay in the exposed class led to a smaller infectious steady, but with the parameters used in Hu et al. (2015), this decrease was negligible. When using a time delay in the infectious class, the infectious steady state increased and, with our parameter values, the increase was significant. This allowed us to conclude that having a time delay in the infectious class has more of an impact on the infectious steady state than having a time delay in the exposed class.

Next, we tested how the magnitude of the time delay affected the infectious steady state. Some diseases will have shorter exposed and infectious periods such as measles and influenza (Hethcote, 2000; Wearing et al., 2005; Safi and Gumel, 2011), and others will have very large periods such as HIV (Anderson et al., 1992). It is important to consider the length of a time delay when selecting the type of distribution needed for a mathematical model. We found that as time spent infectious increases (a larger τ_2), the difference between the two systems' infectious steady states decreases. Therefore, if the disease has a large infectious period, the infectious steady state would be similar for the exponential system and the delay system. In this case, it would be best to use the exponential system due to its simplicity. When doing a similar analysis for the magnitude of the exposed time delay, we saw that the difference

between our two infectious steady states was extremely small. This again emphasizes the importance of the time delay in the infectious class versus the exposed class.

Finally, we investigated how the placement of a control measure affected the impact each time delay had on the infectious steady state. A disease may have multiple possible control measures available. For instance, Ebola does not yet have a vaccine, but it is important to consider quarantining the exposed population, promoting safe burial practices, and hospitalization rates (Hu et al., 2015; Haas, 2014; Pandey et al., 2014; Meltzer et al., 2014; Meltzer, 2016). For this study, we looked at how vaccinating the susceptible class or quarantining the exposed or infectious class would affect the model. We found that placing a vaccination on the susceptible class led to similar results as having a quarantine on the infectious class. The infectious time delay, τ_2 , had a greater impact on the infectious steady state. On the contrary, when a quarantine was applied to the exposed class, the exposed time delay, τ_1 , led to a decrease in the infectious steady state as it approached the delay's infectious steady state. Although the distribution of infectious periods is usually the most important because infectives spread the disease, we suggest that if a control strategy acts directly on a compartment, the distribution of time spent in that compartment becomes similarly important. To understand the impact of a control strategy, it may be necessary to model the timing of that control in detail rather than assuming it is exponentially distributed.

We believe caution must be taken when applying control measures to models using ordinary differential equations. Although simple and quick to analyze, they could lead to significant underestimates or even overestimates in the prediction of the infectious population, causing difficulties in controlling the disease. Future modeling may include yet more types of control measures, such as hospitalization rates and burial practices, along with incorporating death by disease, to better elucidate the role of time distributions spent in each compartment.

2.9 Appendix

2.9.1 Endemic Steady State for Exponential System

The endemic steady state for (2.1) is

$$\begin{aligned}
 S_E^* &= \frac{(\sigma + \mu)(\alpha + \gamma + \mu)}{\beta\sigma} \\
 E_E^* &= \frac{-\mu(\sigma + \mu)(\alpha + \gamma + \mu)}{\beta\sigma(\sigma + \mu)} + \frac{\mu}{\sigma + \mu} \\
 I_E^* &= \frac{\mu}{\alpha + \mu} \left(\frac{\sigma}{\sigma + \mu} \right) \left[1 - \left(\frac{\gamma}{\gamma + \alpha + \mu} \right) \right] - \frac{\mu}{\beta} \\
 Q_E^* &= \frac{-\alpha\mu}{\beta(\gamma + \mu)} + \frac{\sigma\alpha\mu}{(\gamma + \mu)(\sigma + \mu)(\alpha + \gamma + \mu)} \\
 R_E^* &= \frac{-\gamma(\alpha + \gamma + \mu)}{\beta(\gamma + \mu)} + \frac{\gamma\sigma}{(\gamma + \mu)(\sigma + \mu)}
 \end{aligned}$$

where our main focus is on I_E^* .

2.9.2 Endemic Steady State for Delay System

The endemic steady state for (2.2) is

$$\begin{aligned}
 S_D^* &= \frac{e^{\mu\tau_1 + (\alpha + \mu)\tau_2}(\alpha + \mu)}{\beta(e^{(\alpha + \mu)\tau_2} - 1)} \\
 E_D^* &= \frac{(e^{-\mu\tau_1} - 1)((\alpha + \mu)e^{\mu\tau_1 + (\alpha + \mu)\tau_2} - \beta(e^{(\alpha + \mu)\tau_2} - 1))}{\beta(e^{(\alpha + \mu)\tau_2} - 1)} \\
 I_D^* &= \frac{\mu}{\alpha + \mu} e^{-\mu\tau_1} [1 - e^{-(\mu + \alpha)\tau_2}] - \frac{\mu}{\beta} \\
 Q_D^* &= \frac{e^{-\mu\tau_1 - (\alpha + \mu)\tau_2} [(\alpha + \mu)e^{\mu\tau_1 + (\alpha + \mu)\tau_2} - \beta(e^{(\alpha + \mu)\tau_2} - 1)] [\alpha e^{\alpha\tau_2} (1 - e^{\mu\tau_2}) + \mu(e^{\alpha\tau_2} - 1)]}{\beta(\alpha + \mu)(e^{(\alpha + \mu)\tau_2} - 1)} \\
 R_D^* &= \frac{\beta(1 - e^{\tau_2(\alpha + \mu)}) + (\alpha + \mu)e^{\mu\tau_1 + \tau_2(\alpha + \mu)}}{\beta e^{\mu(\tau_1 + \tau_2)} [1 - e^{\tau_2(\alpha + \mu)}]}
 \end{aligned}$$

where our main focus is on I_D^* . Recall $\tau_1 = \frac{1}{\sigma}$ and $\tau_2 = \frac{1}{\gamma}$.

2.9.3 R_0 for Multi-Infected Compartment Model

Using the method established by Van den Driessche and Watmough (2002), we find the basic reproduction number, R_0 , for the multi-infected compartment model, (2.3). First, note that there are $n + 2m$ infected compartments: $E_1, E_2, \dots, E_n, I_1, I_2, \dots, I_m$, and Q_1, Q_2, \dots, Q_m . Therefore, $(n + 2m) \times (n + 2m)$ matrices are needed such that \mathcal{F} is the new infections matrix and \mathcal{V} holds the negative of all other terms. Using all equations of the system, we obtain

$$\mathcal{F} = \begin{pmatrix} 0 \\ BS \sum_{i=1}^m I_{M,i} \\ 0 \\ \vdots \\ 0 \\ 0 \\ 0 \\ \vdots \\ 0 \\ 0 \\ 0 \\ \vdots \\ 0 \\ 0 \end{pmatrix}$$

and

$$\mathcal{V} = \begin{pmatrix} -\mu + BS \sum_{i=1}^m I_{M,i} + \mu S \\ (\mu + n\sigma)E_1 \\ -n\sigma E_1 + (\mu + n\sigma)E_2 \\ \vdots \\ -n\sigma E_{n-1} + (\mu + n\sigma)E_n \\ -n\sigma E_n + (\mu + \alpha + m\gamma)I_1 \\ -m\gamma I_1 + (\mu + \alpha + m\gamma)I_2 \\ \vdots \\ -m\gamma I_{m-1} + (\mu + \alpha + m\gamma)I_m \\ -\alpha I_1 + (\mu + m\gamma)Q_1 \\ -\alpha I_2 - m\gamma Q_1 + (\mu + m\gamma)Q_2 \\ \vdots \\ -\alpha I_m - m\gamma Q_{m-1} + (\mu + m\gamma)Q_m \\ -\gamma(I_m + Q_m) + \mu R \end{pmatrix}.$$

Next, using only the infected compartments, the derivative submatrices at the disease free equilibrium are calculated to be

$$F = \begin{pmatrix} 0 & 0 & \cdots & 0 & \beta & \beta & \cdots & \beta & 0 & 0 & \cdots & 0 \\ 0 & 0 & \cdots & 0 & 0 & 0 & \cdots & 0 & 0 & 0 & \cdots & 0 \\ \vdots & \vdots & \ddots & \vdots & \vdots & \vdots & \ddots & \vdots & \vdots & \vdots & \ddots & \vdots \\ 0 & 0 & \cdots & 0 & 0 & 0 & \cdots & 0 & 0 & 0 & \cdots & 0 \end{pmatrix}$$

and

$$V = \begin{pmatrix} \mu + n\sigma & 0 & 0 & \cdots & 0 & 0 & 0 & \cdots & 0 & 0 & 0 & \cdots & 0 \\ -n\sigma & \mu + n\sigma & 0 & \cdots & 0 & 0 & 0 & \cdots & 0 & 0 & 0 & \cdots & 0 \\ 0 & -n\sigma & \mu + n\sigma & \cdots & 0 & 0 & 0 & \cdots & 0 & 0 & 0 & \cdots & 0 \\ \vdots & \vdots & \vdots & \ddots & \vdots & \vdots & \vdots & \ddots & \vdots & \vdots & \vdots & \ddots & \vdots \\ 0 & 0 & 0 & \cdots & \mu + n\sigma & 0 & 0 & \cdots & 0 & 0 & 0 & \cdots & 0 \\ 0 & 0 & 0 & \cdots & -n\sigma & \mu + \alpha + m\gamma & 0 & \cdots & 0 & 0 & 0 & \cdots & 0 \\ 0 & 0 & 0 & \cdots & 0 & -m\gamma & \mu + \alpha + m\gamma & \cdots & 0 & 0 & 0 & \cdots & 0 \\ \vdots & \vdots & \vdots & \ddots & \vdots & \vdots & \vdots & \ddots & \vdots & \vdots & \vdots & \ddots & \vdots \\ 0 & 0 & 0 & \cdots & 0 & 0 & 0 & \cdots & \mu + \alpha + m\gamma & 0 & 0 & \cdots & 0 \\ 0 & 0 & 0 & \cdots & 0 & -\alpha & 0 & \cdots & 0 & \mu + m\gamma & 0 & \cdots & 0 \\ 0 & 0 & 0 & \cdots & 0 & 0 & -\alpha & \cdots & 0 & -m\gamma & \mu + m\gamma & \cdots & 0 \\ \vdots & \vdots & \vdots & \ddots & \vdots & \vdots & \vdots & \ddots & \vdots & \vdots & \vdots & \ddots & \vdots \\ 0 & 0 & 0 & \cdots & 0 & 0 & 0 & \cdots & -\alpha & 0 & 0 & \cdots & \mu + m\gamma \end{pmatrix}.$$

Then taking the product of F and V^{-1} yields an upper triangular matrix of

$$FV^{-1} = \begin{pmatrix} \beta \left(\frac{n\sigma}{\mu + n\sigma} \right)^n \left(\frac{1}{\mu + \alpha + m\gamma} \right) + \cdots + \beta \left(\frac{n\sigma}{\mu + n\sigma} \right)^n \left(\frac{(m\gamma)^{m-1}}{(\mu + \alpha + m\gamma)^m} \right) & \cdots & 0 + \cdots + \beta \left(\frac{(m\gamma)^{m-2}}{(\mu + \alpha + m\gamma)^{m-1}} \right) & \cdots & 0 \\ 0 & \cdots & 0 & \cdots & 0 \\ \vdots & \vdots & \vdots & \ddots & \vdots \\ 0 & \cdots & 0 & \cdots & 0 \end{pmatrix}.$$

Therefore, the only nonzero eigenvalue is

$$\beta \left(\frac{n\sigma}{\mu + n\sigma} \right)^n \left(\frac{1}{\mu + \alpha + m\gamma} \right) \left[1 + \frac{m\gamma}{\mu + \alpha + m\gamma} + \left(\frac{m\gamma}{\mu + \alpha + m\gamma} \right)^2 + \cdots + \left(\frac{m\gamma}{\mu + \alpha + m\gamma} \right)^{m-1} \right].$$

Summing the geometric series, the eigenvalue simplifies to

$$\frac{\beta}{\mu + \alpha} \left(\frac{n\sigma}{\mu + n\sigma} \right)^n \left(1 - \left(\frac{m\gamma}{\mu + \alpha + m\gamma} \right)^m \right),$$

our final R_0 value.

2.9.4 Infectious Steady State with Applying Vaccine on Susceptible Class

The infectious steady state for the multi-infected compartment model with a vaccine applied to the susceptible class (see Fig. 2.8) is

$$\sum_{i=1}^n I_i^* = \left(\frac{n\sigma}{\mu + n\sigma} \right)^n \left(1 - \left(\frac{m\gamma}{\mu + m\gamma} \right)^m \right) - \frac{\mu + \nu}{\beta}. \quad (2.23)$$

The delay system's infectious steady state is

$$I^* = e^{-(\mu+\alpha)\tau_1} (1 - e^{-\mu\tau_2}) - \frac{\mu}{\beta}. \quad (2.24)$$

2.9.5 Infectious Steady States with Applying Quarantine on Exposed Class

The infectious steady state for the multi-infected compartment model when a control measure, quarantine, is applied to the exposed class rather than the infectious class (see Fig. 2.9) is

$$\sum_{i=1}^m I_i^* = \left(\frac{n\sigma}{\mu + \alpha + n\sigma} \right)^n \left[1 - \left(\frac{m\gamma}{\mu + m\gamma} \right)^m \right] - \frac{\mu}{\beta}. \quad (2.25)$$

The delay system's infectious steady state is

$$I^* = e^{-(\mu+\alpha)\tau_1} (1 - e^{-\mu\tau_2}) - \frac{\mu}{\beta}. \quad (2.26)$$

Chapter 3

The Effect of Kin Recognition on Competition Among Clones in Spatially Structured Microbial Communities ¹

3.1 Introduction

Cooperation can require individuals to engage in behaviors that are costly to themselves, while beneficial to others (West et al., 2007). Communities that exhibit cooperative behaviors tend to be susceptible to cheaters, individuals that benefit from cooperators but do not contribute back to the community (Brown et al., 2009; West et al., 2007).

Gaining resources allows cheaters to have a higher reproductive rate, letting them reproduce faster and eventually outcompete the cooperators (West et al., 2007). Despite the potential for invasion by cheaters, cooperative behaviors are prevalent in natural systems. Many cooperative behaviors can be explained through kin selection: individuals cooperate

¹Paper in Preparation: The Effect of Kin Recognition on Competition Among Clones in Spatially Structured Microbial Communities. A. Bingham, A. Sur, L. B. Shaw, and H. Murphy

with relatives who likely share genes for cooperative behavior. If the fitness benefits of cooperating are large enough, the frequency of the cooperative allele will increase in the population, such that cooperation will outcompete other social behaviors (Hamilton, 1964)

One way to ensure the stability of kin selection is through kin recognition (Nadell et al., 2010; West et al., 2007). In kin recognition, an individual determines if another individual is related and therefore can cooperate exclusively with relatives (?). There are many examples of cooperative behavior that rely on kin recognition: bees protecting their queen, ants relying on chemical cues to protect their kin, or fish using scent to follow parents in a stream (Waldman, 1988).

Cooperation and kin recognition have been widely studied in animals and plants. In recent years, studies have begun to focus on microbial communities (Strassmann et al., 2011; Cao and Wall, 2017; Stefanic et al., 2015; Vos and Velicer, 2009; Hirose et al., 2011; West et al., 2007). Cooperation among microbes often occurs through kind recognition where individuals are able to recognize other cooperators through expression of particular genes, known as greenbeards. The term “greenbeard” stems from Dawkin’s *The Selfish Gene* where he gives the example that individuals with green beards only cooperate with those that also have green beards. However, some species are able to take this further and actually distinguish kin, or closely related genetic lineages (Gardner and West, 2010). One example of a microbial species that utilizes kin recognition is the social amoebae *Dictyostelium discoideum*, a eukaryote that is found in soil and prey on bacteria. When starved, cells will sacrifice themselves to form stalks of dead cells that hold fertile spores above the surface and closer to resources (Strassmann et al., 2011; Hirose et al., 2011). By recognizing kin through transmembrane proteins, cells ensure that they are sacrificing themselves for kin and that cheaters are not taking advantage of their sacrificial behavior (Hirose et al., 2011; Noh et al., 2018).

A ubiquitous cooperative microbial behavior is the formation of biofilms, a microbial community that attaches to a surface and is protected by an extracellular matrix. Biofilms are highly studied due to their threats to human health and industry. They can be found

in hospital settings, such as catheter implants, and lead to infections (Nadell et al., 2016, 2008). They can also contaminate drinking water. Additionally, biofilms can grow in industrial settings, proving costly to remove (Nadell et al., 2016, 2008). Biofilms are cooperative communities, sharing resources such as a protective extracellular matrix or other “public goods” (Xavier and Foster, 2007; Nadell et al., 2008; Brown et al., 2009; West et al., 2007). In principle, cheaters are a threat to these communities as they could benefit from the extracellular matrix or public goods without expending energy to help produce the public goods. This gives them a higher growth rate and an advantage in outcompeting the cooperators (Nadell et al., 2008; Brown et al., 2009).

The lack of cell movement in biofilms leads to a spatial component that suggests kin selection is inevitable due to the fact that when cells divide, they divide in close proximity to other kin. Therefore, it is likely that a cell’s neighbor is its kin, suggesting that recognition mechanisms are unnecessary (Waldman, 1988). In this way, cooperation can be stable due to the spatial assortment since it leads to cooperation with kin (Xavier and Foster, 2007; Nadell et al., 2010; Momeni et al., 2013). Through direct recognition of kin, we can further limit cooperation to not only cells in the proximity but also to cells that are actually of the same genetic lineage. By cutting off non-cooperators from benefiting from the resources cooperators secrete, non-cooperators do not reproduce as well. This allows cooperators to maintain access to space and nutrients at the edges of the biofilm (Nadell et al., 2016; Kim et al., 2014). Therefore, we explore the possibility that kin recognition provides an extra benefit even in spatially structured cooperative communities.

Eukaryotic cells have the ability to engage in complex communication, as has been shown with *D. discoideum*. It is therefore possible that kin recognition could evolve in eukaryotic microbes, if there is a benefit to it. In fact, there is evidence that kin recognition exists in *Saccharomyces cerevisiae*, the common baker’s yeast (Smukalla et al., 2008). We therefore simulate a generic biofilm inspired by the biology of *S. cerevisiae*. Our simulation is helpful for prediction of biofilms in the natural setting as not much research has been conducted in this area (Strassmann et al., 2011; Noh et al., 2018).

Mathematical models have proven beneficial in studying social interaction in biofilms. In Nadell et al. (2010), they look at diffusion of resources and cell growth in bacterial colonies. In Xavier and Foster (2007), they use an individual based model to look at how social interactions in biofilms affect the contribution and diffusion of the extracellular polymeric substances, which protect the biofilm. Our simulations are modeled after Momeni et al. (2013), where they use a three-dimensional, agent based model for the growth of two yeast strains. Though they captured the idea of obligate cooperation, they did not study kin recognition as their model did not include the effect that cells have on others of the same type. Additionally, they only considered periodic boundary conditions rather than outward expansion of a colony cell growth. Through the use of mathematical simulations, we investigate how varying the cooperation strength, the initial proportion of cooperators in the colony, and the density of the colony affects cooperators' ability to be successful in growing in a biofilm in a colony. In each case, we quantify how much more successful kin recognition makes cooperators than when cooperators allow cheaters to benefit from their resources. To our knowledge, this is the first spatial simulation to incorporate kin recognition.

In Section 3.2, we describe how we can simulate various social interactions by varying parameters in a cell's growth rate. We also describe the overall agent based model and measurements we take throughout the simulation. Section 3.3.1 shows the total proportion of cooperators at the end of each social interaction we investigate, while Section 3.3.2 reveals how much cooperators benefit from expressing kin recognition. Then, in Section 3.3.3, we compare how differing colony densities affect the benefit to kin recognition. We discuss our findings and conclude in Section 4.4.

3.2 Methods

We introduce an agent based model to study the interactions between two yeast strains in a colony. Cells are placed on a three-dimensional cubic array. To model cell growth occurring in continuous time, the simulation uses a discrete time Monte Carlo method with

a small time step and random sequential update. At each update, a random cell is selected, the probability it will divide is determined, and if it divides, a daughter cell is placed at a nearby location. This process continues until a designated stopping point. Social interactions are implemented by altering the rate at which a cell divides and taking into consideration the competition within the neighborhood.

The growth rates for the two cell types, cooperators (C) and non-cooperators (N), are

$$r_C = (r_{C0} + r_{CN}\phi_N + r_{CC}\phi_C) [1 - \chi(\phi_C + \phi_N)], \quad (3.1)$$

$$r_N = (r_{N0} + r_{NC}\phi_C + r_{NN}\phi_N) [1 - \chi(\phi_C + \phi_N)], \quad (3.2)$$

respectively. Parameters and variables are listed in Table 3.1 and are explained below.

Each cell type starts with a baseline growth rate, r_{C0} or r_{N0} , when unaffected by social interactions. We will usually assume that the baseline growth rate for non-cooperators is higher than that of cooperators because the cooperator cells are redirecting some energy to produce a public good rather than toward their own growth.

To determine the effect of social interactions on a cell, we must calculate the occupancy fraction of each cell type that surrounds a focal cell. The occupancy fraction of cooperators, ϕ_C , is the number of cooperator cells in a cube of volume $(2R_i + 1)^3$ centered at the focal cell, divided by the volume $(2R_i + 1)^3$. Here R_i is the interaction radius. The occupancy fraction of non-cooperators, ϕ_N , is defined similarly. If a cell is near the boundary of the cubic array, we divide by the actual volume that surrounds the cell and is part of the array. The occupancy fractions lie between 0 and 1. It is worth noting that calculating the occupancy fraction can become computationally expensive so we reduce how often it is calculated (see Appendix 3.5.1).

| Parameter | Meaning | Value |
|------------|---|--------------------------|
| r_C | Cooperator cell growth rate | Calculated in simulation |
| r_N | Non-cooperator cell growth rate | Calculated in simulation |
| r_{C0} | Baseline growth rate for cooperators | 0.05 |
| r_{N0} | Baseline growth rate for non-cooperators | 0.1 |
| r_{CC} | Social effect of cooperators on themselves | 0, 0.1, 0.3, 0.5, 0.7 |
| r_{NC} | Social effect of cooperators on non-cooperators | 0, 0.1, 0.3, 0.5, 0.7 |
| r_{NN} | Social effect of non-cooperators on themselves | 0 |
| r_{CN} | Social effect of non-cooperators on cooperators | 0 |
| χ | Competition effect | 1 |
| ϕ_C | Occupancy fraction of cooperators in neighborhood | Calculated in simulation |
| ϕ_N | Occupancy fraction of non-cooperators in neighborhood | Calculated in simulation |
| N_c | Maximum biofilm length and width | 50 |
| N_z | Maximum biofilm height | 100 |
| T | Maximum number of simulated cells grown | 50000 |
| d | Initial droplet length | 15 |
| f | Fraction of droplet filled with cells | 0.05 |
| f_C | Fraction of inoculated cooperator cells | 0.3, 0.5, 0.7 |
| R_i | Interaction radius | 3 |
| R_d | Displacement radius | 3 |
| Δt | Time step | 0.1 |

Table 3.1 Parameters used to simulate biofilm inoculation and cell growth.

Social interactions other than competition are set by the parameters r_{ij} (where i is C or N and j can be the same or opposite). The effect that cooperators have on themselves is determined by r_{CC} , and the effect that non-cooperators have on themselves is determined by r_{NN} . Then, the effect that non-cooperators have on cooperators is r_{CN} , and the effect that cooperators have on non-cooperators is r_{NC} . Normally, non-cooperators will have no effect on cooperators or each other, so $r_{NN} = r_{CN} = 0$.

We also incorporate a competition effect χ . We set $\chi = 1$ so that the final factor in the growth rates, $1 - \chi(\phi_C + \phi_N)$, turns off growth when the neighborhood is full.

We can now vary the growth rate parameters to simulate various social interactions. We consider three scenarios: baseline competition, simple cheating, and cooperation with kin recognition. For baseline competition, which we use as a reference point, all social inter-

actions other than competition are turned off ($r_{CC} = r_{NN} = r_{CN} = r_{NC} = 0$). For simple cheating (or cooperation without kin recognition), both $r_{CC}, r_{NC} > 0$. We set $r_{NC} = r_{CC}$ so that cheaters derive the same benefit from cooperator neighbors that another cooperator would. Lastly, to simulate kin recognition, we again set $r_{CC} > 0$. However, the non-cooperators do not benefit from the public goods that cooperators produce so $r_{NC} = 0$.

We begin the simulation with inoculation of a diluted droplet of cells into a small square at the center of the bottom layer of our cubic array (see Fig. 3.1). This allows us to simulate outward expansion of an initial colony, in contrast to the simulation in Momeni et al. (2013) with random inoculation throughout their whole bottom layer. The size of the cubic array is 50 cells (x-direction) by 50 cells (y-direction) with a height of 100 cells (z-direction). The initial square has dimensions $d \times d$, where in our simulations $d = 15$, and a fraction $f = 0.05$ of the sites are randomly selected to fill with cells (rounded down if fd^2 is not an integer). A fraction f_C of the initial cells are randomly assigned as cooperators, and the remainder are non-cooperators.

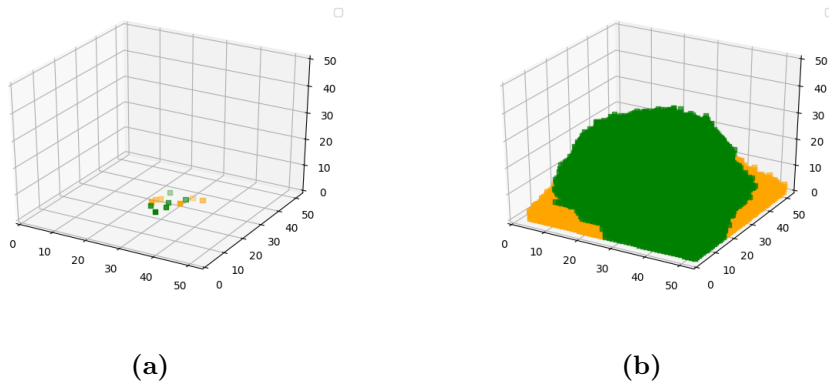


Figure 3.1 (a) Schematic of cells randomly distributed within a centered square droplet on the bottom surface of the cubic array in the simulation. The green squares are cooperators and the orange squares are non-cooperators. This figure depicts a cell inoculation in which $f_C = 0.5$. (b) Schematic of cells at the end of the simulation for which $f_C = 0.5, r_{CC} = 0.5$, and $r_{NC} = 0$.

We next simulate cell growth using a discrete time Monte Carlo algorithm with small time step $\Delta t = 0.1$ and random sequential updating. A cell is selected at random for possible

division. Its growth rate r (either r_C or r_N depending on cell type) is calculated from Eq. ?? and ??, and its probability to grow is $P = r\Delta t$. A uniform random number $0 \leq u < 1$ is generated, and if $u < P$, the cell divides and a daughter cell is placed nearby. For each time step, a random cell selection is made T times, where T is the total number of cells in the colony at the beginning of the time step.

If it is determined that a cell will divide, the next step is to find an empty site for the daughter cell to be placed. We first check the eight sites immediately surrounding the selected cell in the same horizontal plane, giving priority to the four sites directly rather than diagonally adjacent to the cell (see Fig. 3.5a in Appendix 3.5.2). If more than one equidistant empty site is available, we randomly select one of those empty sites.

If the surrounding eight sites are full, we next consider whether the dividing cell will push nearby cells aside horizontally in a planar displacement neighborhood to make room for the daughter cell. We check for empty sites within a square neighborhood of radius R_d in the same horizontal plane (see Fig. 3.5b in Appendix 3.5.2). While Momeni et al. (2013) used a displacement radius equal to 2, their data suggests the it could be as high as 5. We keep track of all the empty sites that are found and calculate the Euclidean distance to each site. We find the minimum distance, and if there are multiple locations at the same distance, we select a random location. The daughter cell is placed adjacent to the parent, pushing the existing cells toward the empty site. A similar mechanism to push nearby cells was implemented by Momeni et al. (2013). See Appendix 3.5.2 for details.

If there are no empty sites in the planar displacement neighborhood, we place the daughter cell directly above the mother cell (see Fig. 3.5c in Appendix 3.5.2) as this has been shown to be a characteristic of *S. cerevisiae* (Momeni et al., 2013). If there are cells above the mother cell, we push them upwards.

We continue simulating cell growth until a stopping point is reached. In most cases, the stopping point will be when the colony reaches a total of 50,000 cells (see Fig. 3.1b), which, through various trials, we have determined gives good representation of a mature biofilm. The bottom of the plate will be over 90% filled and cells throughout the biofilm will have

begun to divide upwards, giving us a three-dimensional structure.

We ran a total of 20 simulations for each combination of parameters, and the average of each measurement was taken over the 20 simulations. Once a cell in the bottom layer touches the outer edge we store the total number of each cell type in the colony. This is to capture a situation in which the colony is not as dense as it will be at the end of the simulation, which will allow us to see effects of cell density. We also store the total numbers at the end of the simulation.

As stated above, growth rates depend on both the social interaction parameters and the neighborhood surrounding the cell. Having a small number of cooperative neighbors increases growth, but having too many will reduce growth due to competition. The advantage of increasing the cooperation parameter r_{CC} is thus not immediately apparent. By differentiating Eq. ?? with respect to occupancy fraction, we find the maximum growth rate a cooperator could achieve, attained when $\phi_C = \frac{r_{CC} - \chi r_{C0}}{2\chi r_{CC}}$ and $\phi_N = 0$, is $r_{C\max} = \frac{(r_{CC} + r_{C0})^2}{4r_{CC}}$. For the parameter values used here, the maximum cooperator growth rate $r_{C\max}$ is monotonically increasing with the cooperation parameter r_{CC} . Also, note that the max growth rate for baseline competition is 0.05, or the basal growth rate for cooperators. For easier interpretation of our results, we plot our simulations versus the maximum possible growth rate of cooperators rather than versus the bare parameter r_{CC} .

3.3 Results

3.3.1 Total Proportion of Cooperators

In order to gain an idea of the dynamics of the simulations, we look at the final average of total proportion of cooperators for kin recognition (blue) and simple cheating (red) in Fig. 3.2. This quantity demonstrates the reproductive ability of each cell type, allowing us to measure the success of cooperators. Note that baseline growth rate is the first data point, $r_{C\max} = 0.05$.

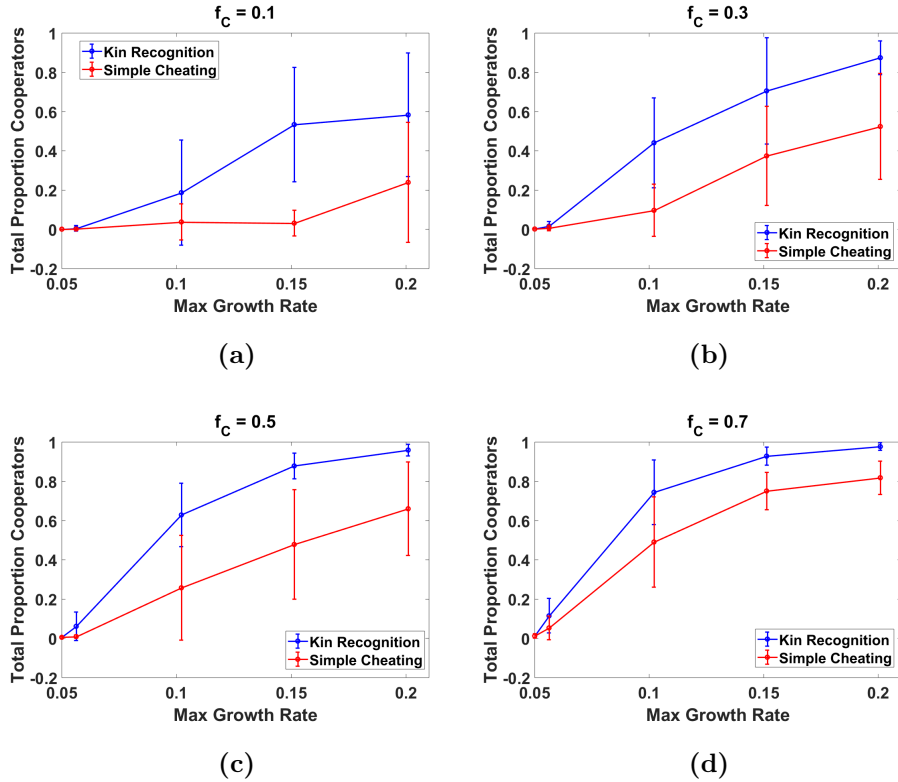


Figure 3.2 Total proportion of cooperators at the end of the simulation for various values of the maximum growth rate for cooperators as cooperation parameter r_{CC} is varied when there is kin recognition (blue) or simple cheating (red), for initial fraction of cooperators at (a) 10 percent, (b) 30 percent, (c) 50 percent and (d) 70 percent. Baseline growth rate is the first data point, $r_{C\max} = 0.05$.

We observe that cooperators do better when expressing kin recognition than when cheaters are able to benefit from their public goods. We also note that cooperators are more successful as their maximum growth rate increases, for both kin recognition and simple cheating. Finally, as the initial fraction of cooperators increases, the total proportion of cooperators saturates more quickly with increasing maximum growth rate.

3.3.2 Benefit to Relatedness

To measure how much cooperators benefit from expressing kin recognition, we find the benefit to relatedness or the difference between total proportion of cooperators when there is kin recognition and total proportion with simple cheating (see Fig. 3.3).

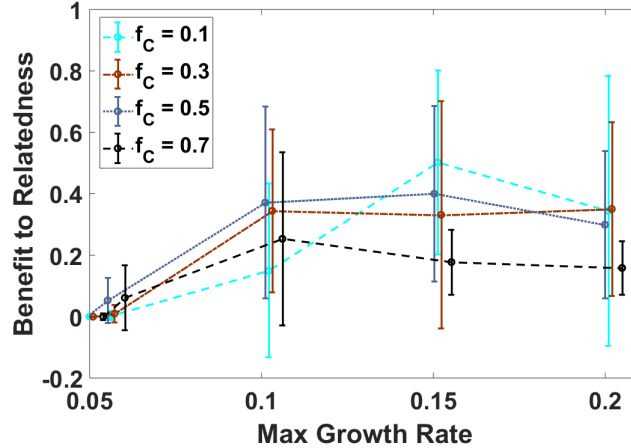


Figure 3.3 Benefit to relatedness for various values of initial proportion of cooperators and maximum growth rate for cooperators. Note that the data points are staggered for display purposes only.

We note that cooperators generally benefit from kin recognition more when they are a moderate fraction (roughly 50 percent) of the cells present. When there are more cooperators (i.e., when $f_C = 0.7$), there are not as many cheaters to take advantage of cooperators, so restricting cooperation only to kin has less of an effect. On the other hand, when the initial proportion of cooperators is 10%, the benefit to relatedness is low for smaller values of max growth rates. This is because cooperators are unable to do as well in either kin recognition or simple cheating scenarios.

The benefit to relatedness seems higher for moderate levels of r_{CC} and, hence, max growth rate. Therefore, for lower values of initial fraction of cooperators, the benefit to relatedness is greater when the maximum growth rate of cooperators is higher.

3.3.3 Sparse Versus Dense Colonies

Lastly, we investigate how the density of the yeast colony affects the benefit to relatedness. While many observations are done in laboratory settings, it is important to predict how cooperators and non-cooperators will interact in more natural settings. As shown in the previous section, when we allow the colony to reach a total of 50,000 cells, it simulates biofilms found in nature since they are able to grow much larger. To simulate the lab setting

of cell growth on a petri dish, we let our simulations run until a cell touches an edge of the cell array on the bottom layer. .

In general, cooperators have a higher total proportion in more dense colonies (see Fig. 3.7 in Appendix 3.5.3). This is because they are surrounded by more of their own kind and are able to benefit from each other. In Fig. 3.4, we see the benefit to relatedness for various initial proportions of cooperators at various maximum growth rates when colonies are sparse (dashed) or dense (solid). The greatest benefit is when the initial fraction of cooperators is 50 percent and when colonies are more dense for maximum growth rates of 0.1 and 0.15. This is because cooperators are more likely to be close to non-cooperators in denser colonies. Therefore, the benefit to cutting off non-cooperators is higher in denser environments. However, we notice that at higher maximum growth rates for cooperators, the benefit can be higher for dense environments.

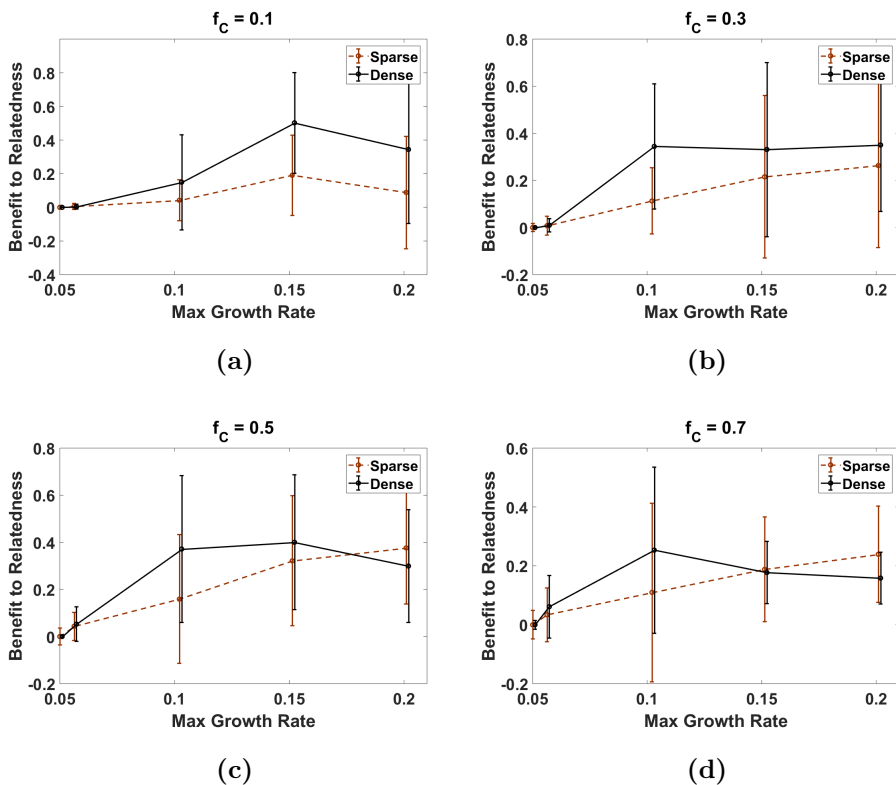


Figure 3.4 Benefit to relatedness for when colonies are sparse (dashed) or dense (solid) compared to maximum growth rate for cooperators at initial proportion of cooperators of (a) 10 percent, (b) 30 percent, (c) 50 percent and (d) 70 percent.

3.4 Conclusion

The study of cooperation and kin recognition has moved into the field of microbiology, revealing that it is possible for eukaryotic cells to express kin recognition (Strassmann et al., 2011; Hirose et al., 2011). We study yeast cell interaction in *Saccharomyces cerevisiae* as they grow and form biofilms. Biofilms can be dangerous for human health since they may grow in the body and on medical implants, making biofilm disruption an important task. However, existing methods such as antibiotics are becoming less effective. We investigate whether cooperators benefit from expressing kin recognition despite already being in a spatially structured colony.

For this study, we have created an agent-based simulation of cell growth with social interactions within a biofilm. By varying parameters for cooperative and non-cooperative growth rate of cells, we can simulate baseline competition for space (where there is no social interaction between the two cell types), simple cheating (where cooperative cells allow non-cooperative cells to benefit without contributing to the production of public goods) and kin recognition (where cooperative cells restrict cooperation to cells that are their own kin or in their genetic lineage).

When simulating the interactions of these two cell types, we focus on varying the effect cooperators have on each other, r_{CC} , and if there is simple cheating, we vary the effect cooperators have on non-cooperators, r_{NC} , at the same rate. Additionally, we look at various values of initial proportion of cooperators, f_C . Finally, we compare measurements taken when looking at sparse versus dense colonies; this is to simulate laboratory settings and natural settings, respectively.

Although cooperators tend to do better when expressing kin recognition, we wanted to quantify how much they benefited over the alternative of allowing simple cheating. While cooperators did increasingly better in both social scenarios as we increased the max growth rate of cooperators and the initial proportion of cooperators, we found that there was a higher benefit to relatedness when the maximum growth rate for cooperators was at intermediate

values. There was also a higher benefit when they had an initial inoculation of 50 percent. For lower initial values of cooperators, the cooperators would benefit more by having a higher cooperative effect. If there is already a high value of initial cooperators, it will not be as beneficial to express kin recognition. Lastly, there is a higher benefit to relatedness in dense communities, which more represents a more natural setting. Once colonies become more dense, there are enough cooperators that they are likely to be next to other cooperators, decreasing the benefit to expressing kin recognition.

Overall, these results allow us to see when cooperative cells benefit the most from kin recognition, which gives insight into the effectiveness of interference by non-cooperative cells. In the future, we would like to conduct spatial analysis on the biofilms in order to view the level of separation between each cell type. Spatial analysis can give us more insight into the dynamics of biofilm formation. Our goal is to use the spatial assortment method outlined by Van Gestel et al. (2014) in which we find the average proportion of cooperator cells that surround a cooperator cell minus the average proportion of cooperator cells that surround a non-cooperator cell. This measurement would allow us to better understand the dynamics in the biofilm.

3.5 Appendix

3.5.1 Calculating the Occupancy Fractions

After selecting a random cell in the cubic array, we must determine the probability the cell will divide. Since we need the occupancy fractions ϕ_C and ϕ_N for the growth rate calculation, looping through a cell's neighborhood repeatedly is computationally expensive, especially when the time steps are small and cells are less likely to divide in smaller time steps. To improve efficiency, we initially compute the occupancy fractions for each cell. They are recomputed only when a cell is considered for division and its neighborhood has been altered. We use a flag for each cell to track whether its occupancy fractions are current or its neighborhood has potentially been altered by movement of nearby cells.

3.5.2 Finding an Empty Site and Cell Movement

We give priority to sites directly adjacent to the dividing cell (Fig. 3.5a) before those that are diagonally adjacent in the same horizontal plane.

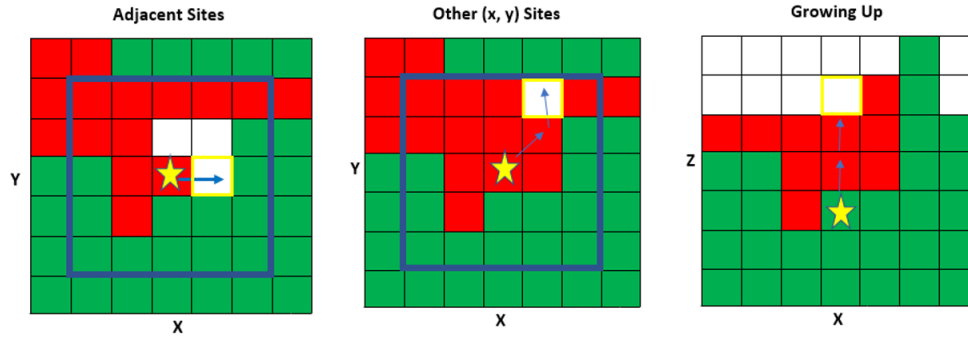


Figure 3.5 (a) A dividing cell (star) places daughter cell into a horizontally adjacent empty site. (b) A dividing cell finds the optimal path and accordingly pushes the cells on the path to the empty site, to create space to place its daughter. (c) A dividing cell places daughter directly upwards. The blue square in (a) and (b) is the interaction neighborhood. In these figures, $R_d = 2$.

If there are no empty adjacent sites available, we check to see if there are sites available within a displacement radius, R_d (Fig. 3.5b). If so, we determine the optimal path along which to push cells toward the empty site to create space for the daughter cell. From the dividing cell, we consider three adjacent cells: those in the x and y directions and the diagonally adjacent cell. Creating a vector from the dividing cell to each of those three cells, we determine which vector is most parallel to the vector from the dividing cell to the empty cell (see Fig. 3.6). While the algorithm defined in Momeni et al. (2013) focused on distance and angle, our algorithm focuses on making sure we remain as parallel as possible to the shortest path to the chosen empty site.

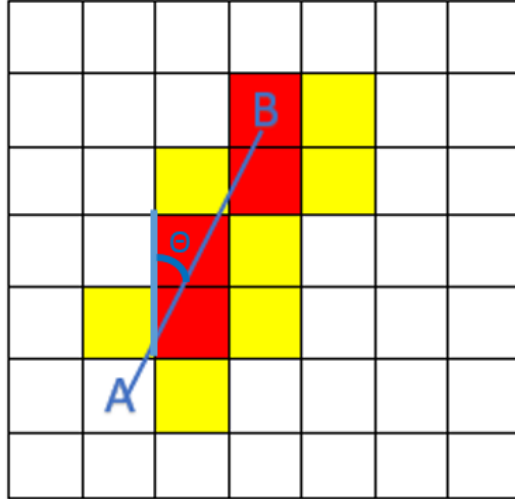


Figure 3.6 Finding the optimal path from a dividing cell at site A to an empty site B. The optimum path is along the red sites, and the yellow sites are the neighboring sites considered.

To do this, we find the cosine of the angle between each vector and the main vector to the empty site. The cosine of each angle is calculated using the magnitudes and dot products of each of the three vectors and the main vector. The vector that creates the smallest angle, or the largest cosine value, will be the direction we select to move closer to the empty site. If there is more than one direction with the maximum cosine value, we randomly choose between them. Having selected the first cell to be pushed by the daughter cell, we record its location. Next, we repeat the process to find the destination of the cell being pushed toward the empty site. We continue finding cells to be pushed in the selected direction until we reach the empty site.

At the end of the algorithm, we return the array of selected directions and move cells away from the dividing cell towards the empty site in the main cubic array. We then place the daughter cell next to the mother cell.

If no empty sites are found on the same plane within the displacement radius, we move up in the z-direction (Fig. 3.5c). Any cells above the dividing cell are pushed upward.

3.5.3 Total Proportion of Cooperators in Various Colony Densities

The total proportion of cooperators is found when colonies are sparse to represent the laboratory setting. A sparse setting is calculated when a cell in the bottom layer first touches an outer edge of the cubic array. Total proportion of cooperators can be seen by the dashed curves in Fig 3.7. For a more dense setting, we use the measurement of total proportion of cooperators at the end of the simulation, when cell totals reach 50,000 cells. This is analogous to a natural setting and is shown by the solid curves. We vary the maximum growth rate for cooperators as well as the initial fraction of cooperators in the inoculation droplet.

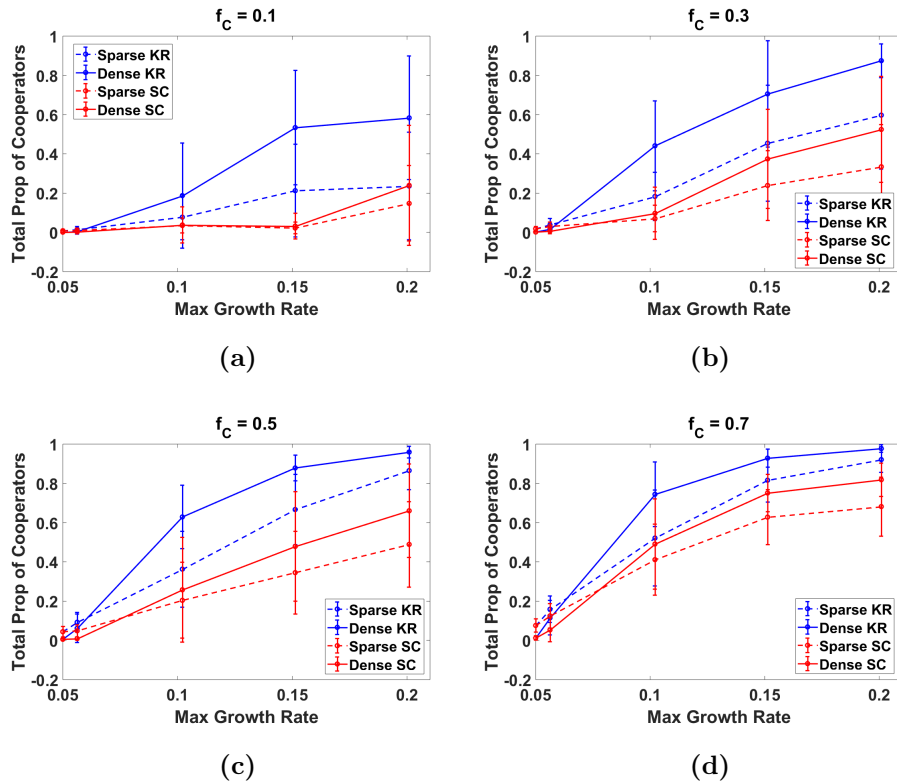


Figure 3.7 Total proportion of cooperators when colonies are sparse (dashed) or dense (solid) for kin recognition (blue) and simple cheating (red) versus maximum growth rate for cooperators at initial proportion of cooperators of (a) 10 percent, (b) 30 percent, (c) 50 percent and (d) 70 percent.

Chapter 4

Two-Patch Organ Model for Competition Between Defective Interfering Particles and Wild-Type Poliovirus ¹

4.1 Introduction

Poliovirus, known to cause poliomyelitis, is a highly contagious and potentially fatal positive-sense single-stranded RNA enterovirus from the Picornaviridae family. Although an oral vaccination containing a live attenuated virus was created by Albert Sabin in the early 1960's (Kew et al., 2005; Kuss et al., 2008; Pfeiffer, 2010), the virus is not yet eradicated and is still endemic in Afghanistan, Nigeria, and Pakistan (Centers for Disease Control and Prevention, 2014; World Health Organization, 2019b; Pfeiffer, 2010). Poliovirus is transmitted via the fecal-oral route (Kew et al., 2005; World Health Organization, 2019b; Kuss et al.,

¹**Paper in Preparation: Two-Patch Organ Model for Competition Between Defective Interfering Particles and Wild-Type Poliovirus. A. Bingham, E. Rousseau, L.B. Shaw, R. Andino, and S. Bianco**

2008; Pfeiffer, 2010; Dowdle and Birmingham, 1997), so the attenuated virus replicates and helps build immunity in the intestine before it is passed. Poliovirus is highly prone to mutations (Racaniello and Baltimore, 1981; Kuss et al., 2008; Kew et al., 2005; Pfeiffer, 2010; Pfeiffer and Kirkegaard, 2006; Dowdle and Birmingham, 1997) , which have been shown to produce reversion of the vaccine strands to virulence.

Defective interfering particles (DIPs) are non-viable defective variants of the wild-type (WT) virus that lack essential functional or structural genes needed to complete the replication cycle. In co-infection with the parent WT virus, they have been shown to produce viable progeny during replication by obtaining the lacking elements from the WT helper virus, reducing the overall WT viral load and essentially acting as a parasite of the WT variant. Once the parent virus population has been depleted, DIPs are incapable of reproducing further. Thus, their use as therapeutics has been long proposed in the literature (Rouzine and Weinberger, 2013; Rast et al., 2016; Marriott and Dimmock, 2010; Huang and Baltimore, 1970; Thompson and Yin, 2010; Huang, 1973). DIPs have been shown to occur naturally in some diseases such as vesicular stomatitis virus (Rouzine and Weinberger, 2013; Huang and Baltimore, 1970), dengue (Rouzine and Weinberger, 2013), and influenza A (Marriott and Dimmock, 2010; Huang and Baltimore, 1970; Huang, 1973) They have rarely been observed in poliovirus natural infections (Wimmer et al., 1993). Shirogane et al. (Shirogane et al., 2019) have engineered a family of DIPs lacking a large portion of the capsid gene. During co-infection, such DIPs have been shown to selectively interfere with the WT virus population by “stealing” the capsid proteins from the WT virus, acting as cheaters (Trono et al., 1988; Rast et al., 2016; Huang, 1973). Moreover, since DIPs are missing genes, their genome is smaller, allowing them to outcompete the WT parent virus during replication (Marriott and Dimmock, 2010).

Mathematical models have been created to follow the competition between DIPs and WT viruses (Rast et al., 2016; Rouzine and Weinberger, 2013; Thompson and Yin, 2010). Thompson and Yin created difference equations to model the interactions of DIPs with vesicular stomatitis virus and found oscillatory dynamics in their experiments (Thompson and

Yin, 2010). Rouzine and Weinberger (2013) investigated the dynamics between therapeutic interfering particles (TIPs) and WT HIV in a cell and extended the model to the host (Rouzine and Weinberger, 2013). Rast et al. extended the model proposed in Rouzine and Weinberger (2013) to include TIP-resistant HIV mutants (Rast et al., 2016). Shirogane et al. (2019) created an intercell model to investigate the dynamics of DIPS and poliovirus among cells in an organ (Shirogane et al., 2019).

This study focuses on following the competition between DIPs and WT poliovirus in two organs as they travel from one organ (such as the intestine) to another (such as the central nervous system) in a two-patch inter-organ model. The aim of our work is to understand the dynamical conditions defining the competition process at this scale of investigation. By changing parameter values and initial conditions we can simulate different scenarios and find parameter values needed for lowering the WT population. In Section 4.2, we introduce the two-patch model and the state variables, parameter definitions, and values. In Section 4.3, we analytically find the eigenvalues associated with the disease free state and show that DIP intervention cannot clear the free WT virus particles completely from the host without some other form of intervention. We also show various simulations based on changed parameter values and initial conditions. Next, we investigate various parameters and their effect on how successful DIPs are in lowering the WT population. Lastly, we explore the system for oscillatory dynamics by varying parameter values. In Section 4.4, we are able to simulate various scenarios of DIP intervention, discover oscillatory dynamics in the model, and investigate how various parameters affect the competition between WT and DIPs in a host.

4.2 Methods

We develop a deterministic two-patch model, simulating the competition between DIPs and their WT parental poliovirus in two organs of specific tissue characteristics, each organ being represented as a patch (see Fig. 4.1). This model is an extension of the single-organ

level, cell-to-cell model developed by Shirogane et al. (Shirogane et al., 2019), and describes the evolution of the number of free DIPs (V_D^i) and WT (V_W^i) virions, as well as of the number of cells that are susceptible (S^i), infected only with WT (I_W^i), infected only with DIPs (I_D^i), or dually infected with both WT and DIPs (I_{DW}^i) in organ i , with $i = A$ or B . The model is composed of the following set of ordinary differential equations:

$$\left\{ \begin{array}{l} \frac{dS^i}{dt} = b - (d + k^i V_W^i + k^i V_D^i) S^i \\ \frac{dI_D^i}{dt} = k^i V_D^i S^i - k^i V_W^i I_D^i - d' I_D^i \\ \frac{dI_W^i}{dt} = k^i V_W^i S^i - k^i V_D^i I_W^i - \delta I_W^i \\ \frac{dI_{DW}^i}{dt} = k^i V_D^i I_W^i + k^i V_W^i I_D^i - \delta I_{DW}^i \\ \frac{dV_W^i}{dt} = n_{\text{out}}^i \delta (I_W^i + \psi^i I_{DW}^i) - n_{\text{in}}^i k^i V_W^i (S^i + I_D^i) \\ \quad - c^i V_W^i - \alpha_{ij} V_W^i + \alpha_{ji} V_W^j \\ \frac{dV_D^i}{dt} = \psi^i \rho^i n_{\text{out}}^i \delta I_{DW}^i - \gamma^i n_{\text{in}}^i k^i V_D^i (S^i + I_W^i) \\ \quad - c^i V_D^i - \alpha_{ij} V_D^i + \alpha_{ji} V_D^j, \end{array} \right. \quad (4.1)$$

where the superscript j represents the other organ compared to i (i.e. if $i = A$ then $j = B$, and if $i = B$ then $j = A$). The production rate of susceptible cells is b and their natural death rate is d . The death rate of cells infected only with DIPs is d' and the death rate of cells infected only with WT or dually infected is δ .

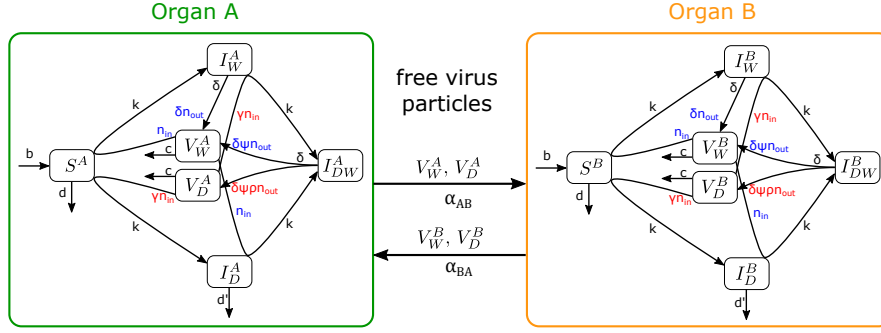


Figure 4.1 Flow chart of the two-patch model. The outer squares represent two different organs. The smaller squares in each organ represent categories of cells (susceptible, infected with WT, DIPs, or dually) and of virus particles (WT and DIPs). Arrows represent interactions among cells and virus particles where parameters in red are for DIP interactions and blue are for WT interactions. Free DIPs and WT particles flow between organs at rate α_{AB} or α_{BA} .

Susceptible cells become infected either with WT or DIPs at a rate k . These singly infected cells can then become dually infected with both WT and DIPs at the same rate k , where each organ has its own rate k . Since not all virus particles are infectious, i.e., able to infect a cell, n_{in} represents the total number of virus particles needed to infect one cell.

WT virus particles are produced from singly infected cells at rate δn_{out} , the product of the cell lysis rate and the WT burst size from singly infected cells. They are also produced from dually infected cells at rate $\psi \delta n_{out}$, where ψ is the ratio of WT burst size from dually to singly infected cells. Additionally, DIPs are produced from dually infected cells at rate $\rho \psi \delta n_{out}$, where ρ is the ratio of DIPs to WT particles produced from dually infected cells. Parameter values are shown in Table 4.1 and are derived from individual experiments or from literature. All simulations begin with 1×10^6 initial susceptible cells (ThermoFisher Scientific, 2019) and no infected cells.

| Parameter | Definition | Value | Source |
|--------------------------------------|---|---|---------|
| b | Production of susceptible cells | $10^6 * \frac{1}{24} (\text{c} \times \text{h})^{-1}$ | 1 |
| d | Death rate of susceptible cells | $\frac{1}{24} \text{h}^{-1}$ | 2 |
| k^A, k^B | Infectivity rate | $5 \times 10^{-8} (\text{p} \times \text{h})^{-1}$ | 3 |
| d' | Death rate of DIP-only infected cells | $\frac{1}{9} \text{h}^{-1}$ | 3,4 |
| δ | Cell lysis rate | $\frac{1}{9} \text{h}^{-1}$ | 5,6 |
| $n_{\text{out}}^A, n_{\text{out}}^B$ | WT burst size from singly infected cells | $10^3 (\text{p} \times \text{c})^{-1}$ | 3,7,8,9 |
| $n_{\text{in}}^A, n_{\text{in}}^B$ | WT virions needed for successful infection | $100 (\text{p} \times \text{c})^{-1}$ | 8,9 |
| ψ^A, ψ^B | WT burst size ratio (dually to singly infected cells) | 0.21 | 3 |
| ρ^A, ρ^B | DIP burst size ratio (DIPs to WT) | 4.14 | 3 |
| c^A, c^B | Virion clearance rate | $\frac{1}{5} \text{h}^{-1}$ | 3 |
| γ^A, γ^B | DIP to WT ratio needed for successful infection | 5 | 3 |
| α_{AB} | Virion migration rate from A to B | 0.001h^{-1} | |
| α_{BA} | Virion migration rate from B to A | 0h^{-1} | |
| S_0^A, S_0^B | Initial number of susceptible cells | 10^6c | 1 |
| $V_{W,0}^A, V_{D,0}^A$ | Initial number of free WT and DIPs in A | 10^3p | |
| $V_{W,0}^B, V_{D,0}^B$ | Initial number of free WT and DIPs in B | 0p | |

Table 4.1 Model parameters and values found in literature and through experiments. Note that A is for rates associated with organ A , B is for rates in organ B , p stands for virus particles, h stands for hours, and c stands for cells. Sources for parameters found in literature are as follows: 1) ThermoFisher Scientific (2019) 2) Rouzine and Weinberger (2013) 3) Shirogane et al. (2019) 4) Regoes et al. (2005) 5) Bird et al. (2014) 6) Burrill et al. (2013) 7) Schulte and Andino (2014) 8) Klasse (2015) 9) Brandenburg et al. (2007)

Since it has been shown that poliovirus usually begins in the intestines and travels to other parts of the body (Kuss et al., 2008; Pfeiffer, 2010; Pfeiffer and Kirkegaard, 2006), and poliovirus is most destructive in the CNS, we can relate organ A to the intestines and organ B to the brain. With traveling from one organ to another comes the issue of a bottleneck. In our case, the bottleneck represents any impedance a virus particle may face as it travels to the other organ. This is one of the more complicated aspects to model as it can be caused by various reasons such as variations in humidity levels, temperature, pH levels, and interferon response (Pfeiffer, 2010; Kuss et al., 2008). Scientists are not sure what path poliovirus takes from the intestine to the CNS, but there is a strong bottleneck from tissues to the

brain, especially from the intestine (Pfeiffer and Kirkegaard, 2006). This makes it difficult to find an approximate value in the literature. Despite the bottleneck being a stochastic process (Kuss et al., 2008), we simplify the model and allow free virus particles to travel from one organ to the other at a constant per capita rate. This process is represented by the free virion migration rates α_{ij} from organ i to organ j . Through trial and error, we choose $\alpha_{AB} = 0.001$. In most cases, since we do not know if it is biologically feasible for poliovirus to travel from the central nervous system to the intestine, we turn off migration of free virus particles from organ B to organ A by setting $\alpha_{BA} = 0$.

4.3 Results

4.3.1 Stability analysis of disease free equilibrium

We investigate whether the presence of DIPs can clear WT poliovirus infection. If this happens, the DIPs would then be cleared as well after all DIP-infected cells would die, as no new DIPs can be produced in the absence of the WT virus. Therefore, we conduct a stability analysis on the disease free equilibrium. We turn off the virion migration rate from organ B to organ A by setting $\alpha_{BA} = 0$ since this is the most biologically realistic scenario. The disease free state is found to be:

$$(S^{A*}, S^{B*}, I_D^{A*}, I_D^{B*}, I_W^{A*}, I_W^{B*}, I_{DW}^{A*}, I_{DW}^{B*}, V_W^{A*}, V_W^{B*}, V_D^{A*}, V_D^{B*}) = \left(\frac{b}{d}, \frac{b}{d}, 0, 0, \dots, 0, 0 \right).$$

Then, using SageMath (The Sage Developers, 2018), we calculate the Jacobian of the system at the disease free state. The twelve eigenvalues, denoted λ_1 to λ_{12} , can be found in Appendix 4.5.1. Eigenvalues 1 to 8, λ_{1-8} , are always negative, so the disease free state is unstable when:

$$\frac{bk^B (n_{out}^B - n_{in}^B)}{c^B d} > 1 \quad \text{or} \quad \frac{bk^A (n_{out}^A - n_{in}^A)}{(\alpha_{AB} + c^A) d} > 1. \quad (4.2)$$

Note that each of the above criteria depends on parameters associated with a particular

organ. Additionally, due to $\alpha_{AB} \ll c^A$, both criteria are similar. Using the parameter values in Table 4.1, λ_{11} and λ_{12} have real part greater than zero, indicating that the disease free state is unstable. Looking at the infectivity rate, one of the most important parameters as determined in Shirogane et al., when k^A and k^B less than 2.2×10^{-10} virus particles (other parameters are as in Table 4.1), the system will go to the disease free state. Also, when the WT burst size from singly infected cells, which could differ by organ, n_{out}^A and n_{out}^B are less than 104, the disease free state is stable.

An important observation we make here is that the stability of the disease free state does not depend on an parameters specifically pertaining to DIPs. This indicates that DIPs alone are unable to stabilize the disease free equilibrium. In other words, DIPs cannot eradicate the WT poliovirus from the host without another form of intervention, such as the immune system. Therefore, in the following we will focus on lowering the WT steady state. We were unable to obtain an analytic expression for the endemic equilibrium, hence we investigate which parameters will help achieve this goal by simulating various scenarios that we predict are biologically significant.

4.3.2 Simulations

To get a basic understanding of how the model behaves, we first compare simulations without DIPs and with DIPs to observe their effect on WT virus levels. The parameter values and initial conditions are set equal in both organs (see Table 4.1) with $\alpha_{BA} = \alpha_{AB}$. We also assume that the initial WT population is small but nonzero (1000 virus particles in both organs), corresponding to an initial introduction of a virus into a host (see Fig. 4.2a). In this way, the system behaves similarly to a single-patch model due to the parameter symmetries (Shirogane et al., 2019). We note that while the number of virions simulated is not exact due to some arbitrarily assigned (such as γ^i) values and the simplified bottleneck, the qualitative behavior of the model is accurate. Therefore, we want to emphasize the dynamical behavior of the systems rather than particular times and virion counts. We notice an initial peak in the free WT population (blue) before it settles into the endemic steady state. Since

parameter values are equal in both organs, the dynamics of both organs are similar.

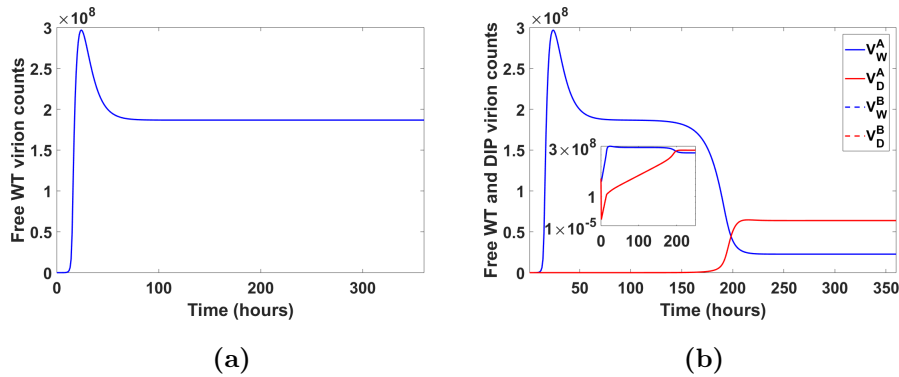


Figure 4.2 (a) Dynamics of number of free WT virions for organ A and B without the interference of DIPs over 360 hours of infection. (b) Reference simulation of two-patch model. (Inset on a log scale.)

Then, in Fig. 4.2b, we introduce an identical amount of DIPs (red) as WT to both organs along with the WT exposure. The introduction of DIPs leads to a two-fold decrease in the steady state free WT virion population in both organs but does not eliminate the WT. To visualize more clearly how the presence of free DIP virions affects the free WT virion population, we include an inset where the free virion population count is on a log scale. Initially, there is a small decrease in the DIP population size. When the WT population is small (as it was at disease onset), the DIP population drops in size since DIPs cannot replicate without WT. Recall that DIPs do not play a role in the stability of the disease free equilibrium as indicated by its eigenvalues. Whenever the WT population is near the disease free equilibrium, the DIP population is eliminated.

Next, we simulate a more biologically realistic scenario of virus particles starting in one organ and moving to the other as the infection progresses (Kuss et al., 2008; Pfeiffer, 2010; Pfeiffer and Kirkegaard, 2006). We do this, as stated in the methods, by setting the initial values of free WT and DIPs virions in organ B to zero and turning off the virion migration from organ B to organ A (i.e., $\alpha_{BA} = 0$). In this scenario, the peak of the WT free virion population occurs slightly later in organ B compared to organ A (Fig. 4.3a). Next, we observe that the free WT and DIP populations in organ B reach a similar steady state to

those in organ A, but at a later time point, indicating that it takes longer for DIPs to lower the WT population in organ B than organ A. Indeed, DIPs need to be established in organ A before large enough numbers move on to organ B and establish themselves there. These results show that it is important to find the right time and best organ to place DIPs in order to prevent damage to the central nervous system.

We also note that the time delay to reach peak WT population size in organ B is not biologically realistic as it takes a few days for poliovirus to reach the brain compared to our couple days (Pfeiffer and Kirkegaard, 2006). In Appendix 4.5.2 we show that the smaller the migration rate between organs becomes, the longer the delay in peak WT population in organ B becomes. As a consequence, there is an even longer delay for the DIPs and WT to reach steady state.

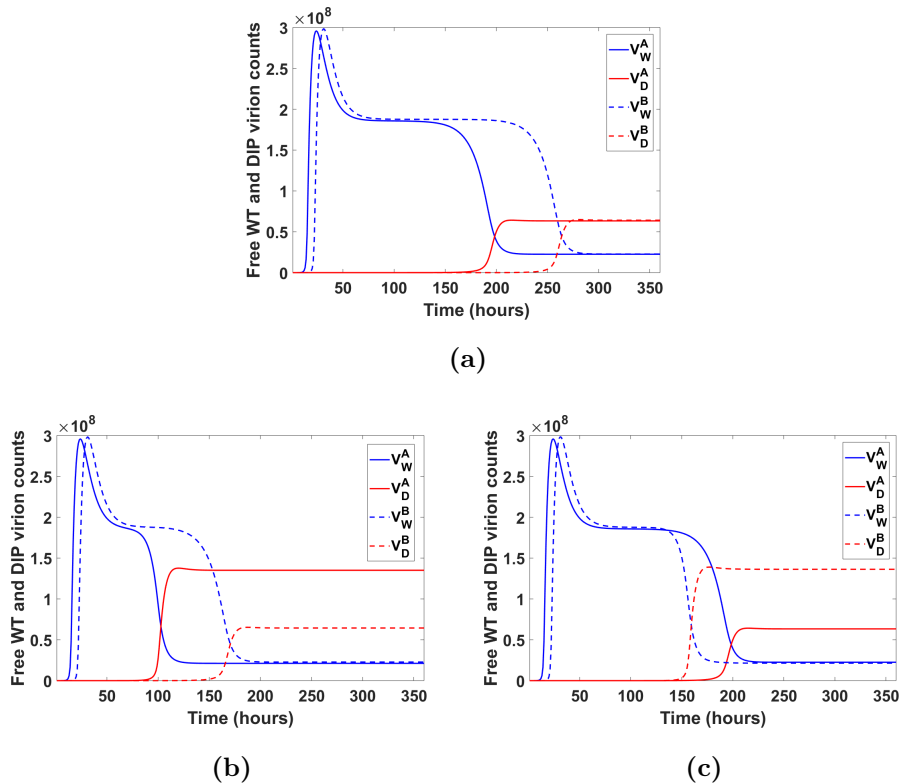


Figure 4.3 (a) Simulation with no initial free WT or DIP virions in organ B. Additionally, we turn off α_{BA} representing no migration of virions from organ B to organ A. (b) Simulation where DIPs are optimized for organ A ($\rho_A = 6$). (c) Simulation where DIPs are optimized for organ B ($\rho_B = 6$). Parameter values can be found in Table 4.1.

We now investigate how changing various parameter values will affect the dynamics. To begin with, we wanted to assess the impact of designing a DIP with higher fitness in either organ A or B on the dynamics, by increasing the relative DIP burst size ρ_A or ρ_B . With an increase in the fitness of DIPs in organ A, the free virion population reaches steady state much more quickly than in the reference simulation, both in organ A and B, indicating that DIPs are more efficient in lowering the WT population (Fig 4.3b). This is promising as it means we can engineer DIPs to be more productive in the initial organ to quickly lower the WT population in both organs.

By increasing the fitness of DIPs in organ B, DIPs lower the free WT virion population in organ B before it is lowered in organ A (Fig 4.3c) and also before it is lowered in the reference simulation. The free WT virion population even has a slightly lower steady state.

Next, we explored the possibility that the actual host environment differs from experimental conditions from which the fitness of the WT virus has been estimated (Shirogane et al., 2019). More specifically, we simulated a scenario in which WT virus particles are less fit in organ A than in organ B. It has been shown that once in the brain, poliovirus particles are able to reproduce without much interference, allowing for a higher number of virus particles to be reached than in other organs (Kuss et al., 2008; Pfeiffer and Kirkegaard, 2006). To simulate this scenario, we lower the WT burst size in singly infected cells in organ A, n_{out}^A , to 300, which also lowers the WT and DIP burst size from dually infected cells in this same organ (see Fig. 4.7 in Appendix 4.5.3). We see that the free WT virion population in organ B still reaches a similar peak size, but that it takes DIPs much longer to lower the WT population. Also, the DIP population in organ A is not able to grow due to the small WT population.

Lastly, we assessed the impact of having less fit DIPs, by lowering DIP burst size in organ A ($\rho_A = 2$, Fig. 4.8a in Appendix 4.5.3) or B ($\rho_B = 2$, Fig. 4.8b in Appendix 4.5.3). In both cases, DIPs are unable to establish in the organ in which their fitness having no effect on lowering the WT population. Also note that lowering the DIP burst size in A also causes a delay in DIPs lowering the WT in B.

4.3.3 Effect of Parameters on DIP Intervention

We have shown that DIPs alone cannot reduce the WT population to extinction. However, we can use DIPs to quickly lower the WT population in order for another form of viral removal to take place, such as the host's immune system. Since we do not yet know how DIPs will react in certain environments or organs, we were curious as to how specific parameters impacted DIPs' ability to lower the WT population. To do this, we looked at the impact parameters in organ B had on the ratio of the number of free WT virions with DIP intervention to without DIP intervention at steady state so that

$$R^i = \frac{V_W^{i*} \text{ with DIP intervention}}{V_W^{i*} \text{ without DIP intervention}}, \quad (4.3)$$

where $i = A, B$. As R^i becomes closer to one, then the free WT virion counts are similar with and without DIPs, and thus DIPs have little effect on lowering the WT population in organ B.

We first looked at how the DIP burst size ratio in organ B, ρ^B , contributed to the effectiveness of lowering the WT population (Fig. 4.4a). As expected, DIPs are less effective for smaller values of ρ^B after a big drop at about $\rho^B = 4$. Also, R^B drops below R^A , indicating that a higher DIP burst size ratio in organ B is more helpful. Note that there is no change in the WT population without DIPs (i.e. the $R^B = 1$ when $\rho_B = 0$) since the WT population does not depend on ρ .

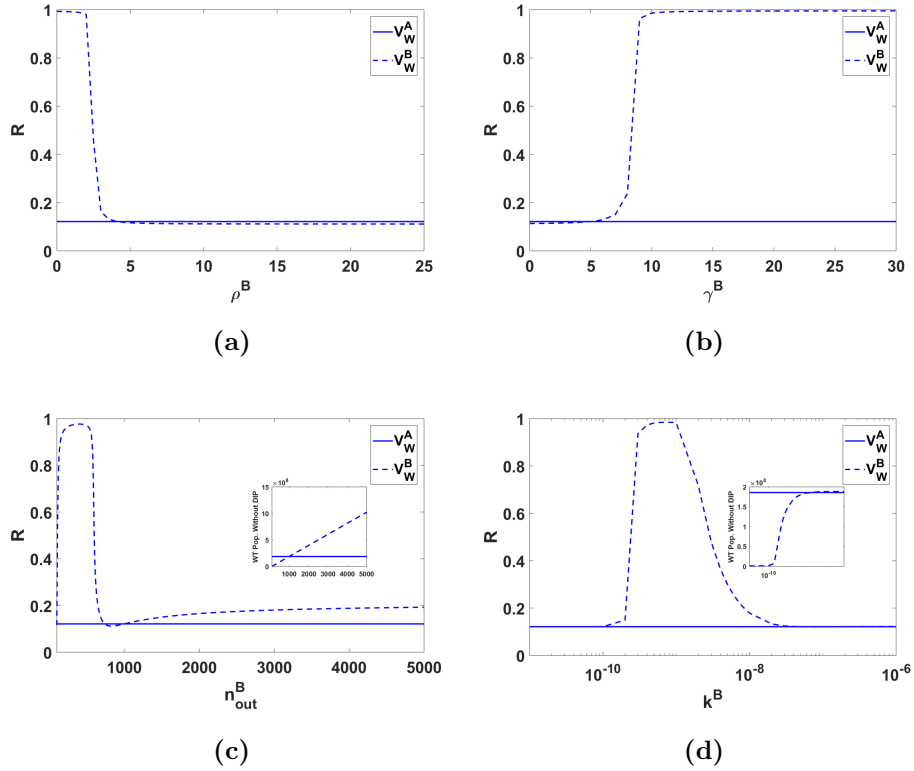


Figure 4.4 Ratio of free WT particles at steady state with DIPs to without DIPs. All parameter values can be found in Table 4.1. Insets indicate change in free WT population without DIP intervention.

Second, we looked at how γ^B , the ratio of DIPs to WT non-infectious to infectious particles, affected DIPs' ability to lower the WT population (see Fig. 4.4b). We see that for larger values of γ^B , DIPs are not as effective. This is because more DIPs are less infectious and more attempts of infection of cells are needed before one particle succeeds.

Third, we show how various values of n_{out}^B affect R^i in Fig. 4.4c. We chose a wider range of values for this parameter as the burst size can get quite large (Schulte and Andino, 2014). We notice that for smaller values of n_{out}^B , DIPs are ineffective. This is because DIPs need WT to reproduce, as shown in Fig 4.7 in Appendix 4.5.3. Then, we notice a sharp decline in R^B before n_{out}^B reaches 1000, then R^B continues to grow as n_{out}^B gets larger. We can see in the inset that the WT population without DIPs continues to rise. Therefore, if we know the WT population in one organ will be particularly small, DIP intervention may not be the best option.

Lastly, we look at the infectivity rate, k^B , which reveals that for smaller values of this parameter, DIPs are effective then become less effective as k^B grows. However, they become effective again after k^B becomes large enough. This “bump” could be do to the fact that too low of an infectivity rate would prevent both WT and DIPs from infecting cells easily, allowing DIPs a chance at outcompeting the WT. Then, at higher values of infectivity, cells are producing more virus particles, which allows for a higher production of DIPs and a better chance at eliminating the WT.

4.3.4 Bifurcation Analysis

We were curious as to whether the system would lead to oscillatory dynamics as found in other models such as the model created for a general WT virus and its DIPs at the cellular level (Huang, 1973) and the model of difference equations for an RNA virus and its DIPs (Thompson and Yin, 2010). Having oscillations in the system could constitute an opportunity to lower the WT population enough so that the immune system can quickly eliminate any remaining virus particles. In order to investigate the dynamics, we ran simulations over a wide range of values for the DIP burst size, ρ^B , and the WT singly infected cell burst size, n_{out}^B . We found that there is a certain range where oscillations do occur by investigating the number of peaks for the WT population in organ B in the last 500 hours (out of a total time of 3500 hours) of each simulation (Fig. 4.5a). In order for something to be defined as a peak (rather than just numerical error), we take the mean of the last 500 time steps and subtract that from the max of the peak. If the difference is greater than 7.5% of the mean, a threshold found through trial and error, we count that as a peak. We find oscillations for values of $\rho^B \geq 10$ and $150 < n_{\text{out}}^B < 450$.

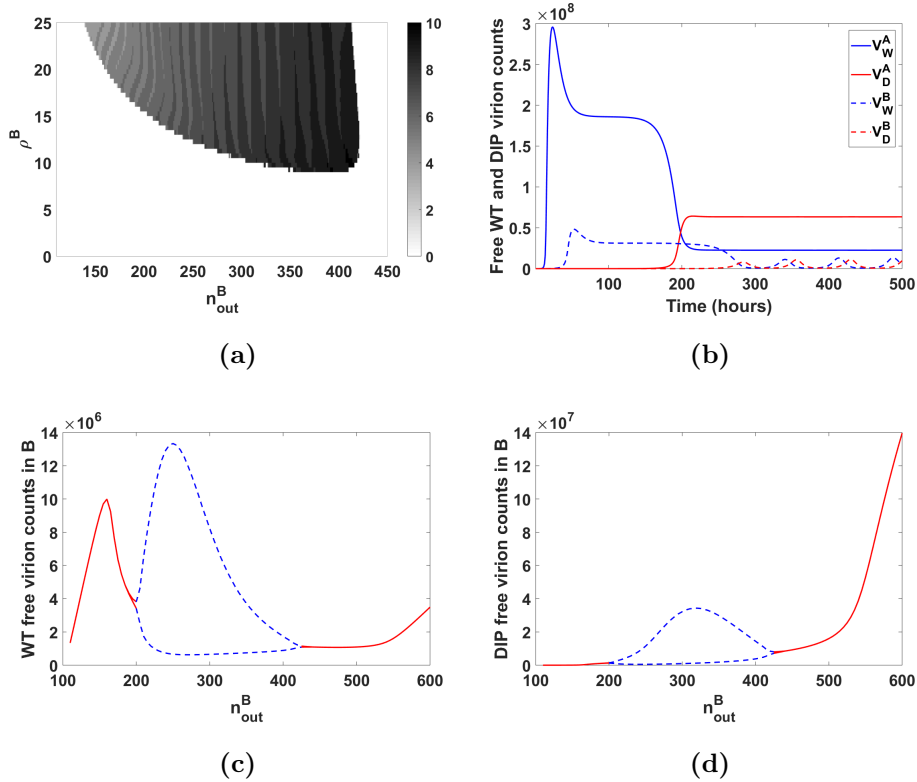


Figure 4.5 (a) Heat map for the number of peaks in WT free virion population in organ B for the last 500 time steps of each simulation as we vary n_{out}^B and ρ^B , where a zero represents no oscillations. Other parameters are set to values found in Table 4.1. (b) Free WT and DIP counts for when $n_{out}^B = 250$ and $\rho^B = 15$. (c-d) Bifurcation diagrams for a range of n_{out}^B values when $\rho^B = 15$. Oscillations are shown in blue. (c) shows the free WT virion count in organ B, and (d) shows the free DIP count.

Using a similar criterion, we created a bifurcation diagram for varying values of n_{out}^B and for $\rho^B = 15$, as the system crosses an oscillatory regime at this parameter value (Fig. 4.5c and Fig. 4.5d). In order to determine where the Hopf bifurcations occur, we run simulations over a range of n_{out}^B values, and take the mean of the last 500 time steps out of 3500 for each simulation. Using the WT population from organ B, if the difference between the maximum value and the mean value from the last 500 time steps is greater than 5% of the mean, we have the first Hopf bifurcation. Once the difference becomes less than 5% of the mean, we have the second. The steady oscillations can be seen in blue in Fig. 4.5b, for $n_{out}^B = 250$. The WT population gets very low in organ B and there are no oscillations in organ A since there is no migration from B to A ($\alpha_{BA} = 0$).

4.4 Conclusion

Poliovirus, a highly contagious disease that can lead to paralysis, is yet to be eradicated worldwide. While vaccines are still being given, they can lead to vaccine-derived polio. In order to find another form of intervention, we investigate the implementation of defective interfering particles to create a competitive environment within a host.

Since the nature of poliovirus depends on differing organ environments and there have been no models developed for the movement of virus particles between organs, we created an inter-organ patch model to measure the competition between defective interfering particles and wild-type poliovirus. By changing parameter values, we were able to simulate various scenarios of DIP intervention. In Fig. 4.2b, we observed that by introducing DIPs into organ A and organ B, the WT population decreased over two-fold. Additionally, we simulated the movement of virus particles from one organ to another by placing zero initial virus particles in organ B and turning off free virus particle migration from organ B to organ A, as shown in Fig. 4.3a. By looking at the eigenvalues of the disease free state, we noticed that we were unable to eradicate WT poliovirus from the host without further intervention. One of the most interesting simulations is when organ A has a higher DIP burst size ratio as shown in Fig. 4.3b. This made both organs reach steady state more quickly, effectively reducing the free WT virus particles more quickly. This indicated that once we know the burst size of the WT population in the initial organ, we can engineer DIPs to have a higher burst size ratio in that organ to quickly lower the WT population in both organs efficiently.

We also investigated how various parameters affected DIPs' effectiveness in lowering the WT population. Smaller values of the DIP burst size ratio led to less effective DIP intervention, as expected. Also, larger values of DIP to WT ratio needed for successful infection led to less DIP effectiveness. This is due to the fact that more DIP particles would be needed for successful lowering of the WT population. Lastly, smaller values of WT burst size from singly infected cells led to less effective DIP intervention as did smaller values of the infectivity rate.

Finally, we discovered stable oscillatory dynamics under a range of values of WT burst size of singly infected cells and DIP burst size ratio. This indicated there is a form of predator prey dynamics in the competition between DIPs and WT poliovirus and that we can lower the WT population for a short range of time so that the host's immune system can more efficiently remove the virus. We also highlighted the Hopf bifurcations for a range of values of WT burst size from singly infected cells for a high value of DIP burst size ratio.

For future work, we would like to create a stochastic model in order to capture a more realistic time delay and bottleneck for the free virion migration from organ A to organ B. It has been suggested by Pfeiffer and Kirkegaard (2006) that a stochastic event would better represent the viral bottleneck. We would also like to incorporate an immune response to see if our model can capture the complete eradication of poliovirus from the host.

4.5 Appendix

4.5.1 Eigenvalues of the Disease Free State

We conduct stability analysis on the disease free equilibrium of our model. Finding the Jacobian at the disease free state (see text), the eigenvalues are as follows:

$$\begin{aligned}
\lambda_{1,2} &= -\delta \\
\lambda_{3,4,5,6} &= -d' \\
\lambda_7 &= -\frac{b\gamma^A k^A n_{in}^A + (\alpha_{AB} + c^A)d}{d} \\
\lambda_8 &= -\frac{b\gamma^B k^B n_{in}^B + c^B d}{d} \\
\lambda_{9,10} &= -\frac{bk^B n_{in}^B + c^B d + d\delta \pm \sqrt{b^2 (k^B)^2 (n_{in}^B)^2 + 4bd\delta k^B n_{out}^B + (c^B)^2 d^2 - 2c^B d^2 \delta + d^2 \delta^2 + 2bdk^B n_{in}^B (c^B - \delta)}}{2d} \\
\lambda_{11,12} &= -\frac{bk^A n_{in}^A + (\alpha_{AB} + c^A) d + d\delta \pm \sqrt{b^2 (k^A)^2 (n_{in}^A)^2 + 4bd\delta k^A n_{out}^A - 2(\alpha_{AB} + c^A) d^2 \delta + d^2 \delta^2 + (\alpha_{AB} + c^A)^2 d^2 - 2bdk^A n_{in}^A (\delta - (\alpha_{AB} + c^A))}}{2d}
\end{aligned}$$

4.5.2 Changing Bottleneck to Prolong Delay to Organ B

Here we investigate various values of α_{AB} in order to see if we can prolong viral entry into organ B to create a more realistic time delay. If we are able to estimate the bottleneck

size and discover that organ B reaches its peak population size rather quickly, we can take preventative steps by injecting DIPs straight into organ B. We vary α_{AB} from 1×10^{-10} to 0.1, to see how this affects the delay between peak WT virion population size (see Fig. 4.6a). We see that as α_{AB} grows larger, there is less time between peak WT free virion counts for each organ. There is a small increase in delay time at $\alpha_{AB} = 0.1$. This is due to organ A reaching its peak sooner since peak WT population in organ A is much smaller than usual. This is because one percent of its population is leaving the organ at every hour.

Additionally, we investigate the difference in time it takes for each organ to reach steady state. To do this, we take the average of the last 500 time steps (out of 1600 hours) for the DIP free virion population. Then, we find the time point where each organ's DIP free virion population size reaches half that average. There is a much larger difference in time it takes each organ to reach this point as α_{AB} becomes smaller.

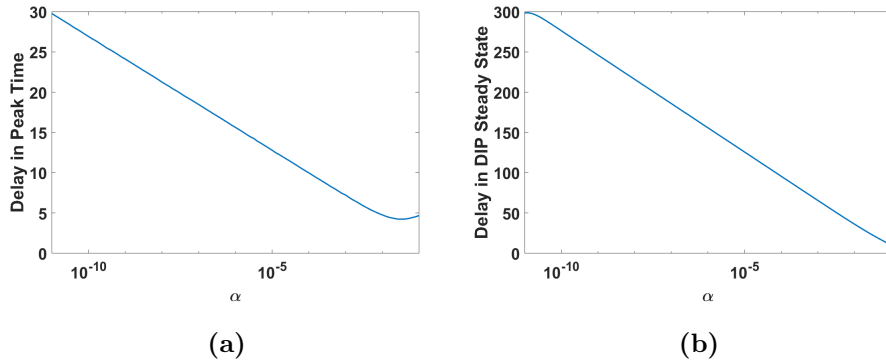


Figure 4.6 (a) How α_{AB} affects the difference in time it takes for each organ to reach peak free WT virions. (b) How α_{AB} affect the difference in time it takes for each organ to reach half its steady state value for DIP free virion count.

4.5.3 Simulation Figures

We investigate other parameter value opportunities that could be biologically realistic. First, we explore what happens if the WT burst size of singly infected cells was lower in organ A than in organ B, $n_{\text{out}}^A = 300$, as it has been shown that once in the brain, poliovirus can produce many virus particles (Kuss et al., 2008; Pfeiffer and Kirkegaard, 2006).

We see that organ A reaches a lower peak for free WT virion population size, and DIPs in organ A are unable to lower the WT population to the same level as the reference simulation (see Fig. 4.7). Again, this is because DIPs need the capsids from WT virions to reproduce. Another important thing to note is that the delay for DIPs to lower the WT population in organ B is much longer. This indicates that if the WT is able to produce more in the brain, then we should find another method to introduce DIPs rather than just into the initial organ.

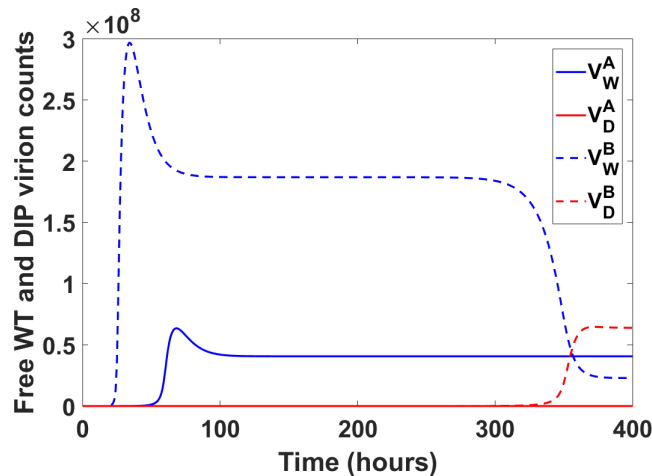


Figure 4.7 Simulation where the WT from singly infected cells are less fit in organ A. We set $n_{\text{out}}^A = 300$.

Lastly, we explore the possibility that DIPs are not efficient in organ A (Fig. 4.8a) or organ B (Fig. 4.8b). When lowered in organ A ($\rho^A = 2$), the DIPs are unable to lower the WT population in organ A, as expected. Note that it also takes a while for the DIP population to lower the WT population in organ B. This is because with few DIPs being produced in organ A, it takes longer for them to travel to organ B. Then, when lowered in organ B, $\rho^B = 2$, we see that the free DIP population in organ B is very small and there is little change to the free WT virion population in organ B. Note that there is also little change to population counts in organ A.

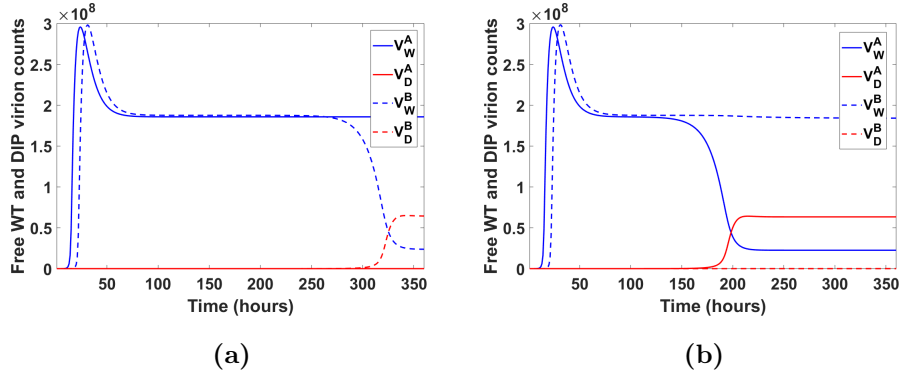


Figure 4.8 (a) Simulation where DIPs in organ A are less fit. We set $\rho_A = 2$. (b) Simulation where DIPs are less fit. We set $\rho_B = 2$.

4.5.4 Delaying DIP Intervention

It is more than likely that we will not know a patient has poliovirus right away. Here, we investigate what happens when we delay DIP intervention. It is also possible that it would be more beneficial to deliver DIPs when the WT has already been established in the population. As we can see in Fig. 4.9, about 10 hours after disease onset DIPs will more quickly lower the WT population. After though, the longer we delay DIP intervention, the longer it will take to lower the WT population. The time for lowering the WT was measured as the time it takes for DIPs to reach half its average steady state value, which was determined by taking the average of the last 500 times points.

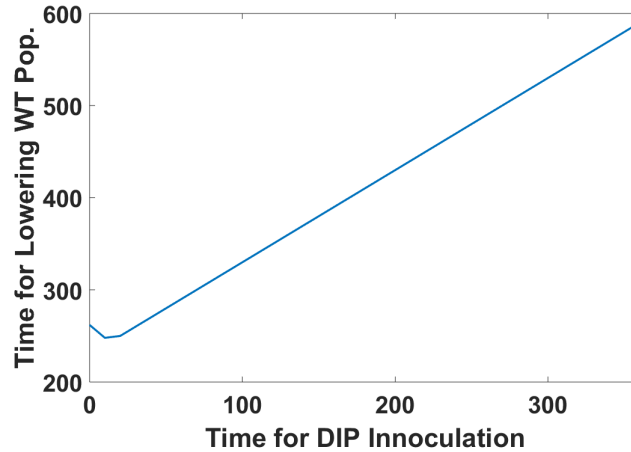


Figure 4.9 Time (in hours) it takes to lower the Wt population as a function of delayed DIP intervention.

Additionally, as can be seen in Fig. 4.10a, time delay of DIP intervention does not affect the difference in time it takes for organ A and organ B to reach peak WT population size. Also, in Fig. 4.10b, we see that it also does not affect the delay in time it takes for DIPs to reach half its steady state population for each organ.

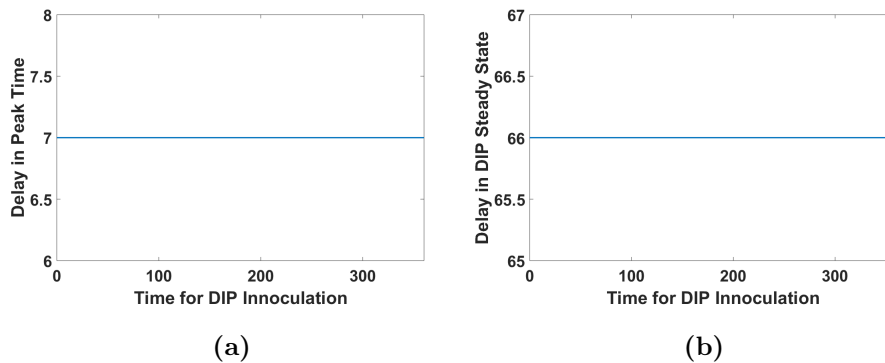


Figure 4.10 (a) How delay in time for DIP intervention affects difference in time (hours) for organ A and organ B to reach peak WT population. (b) How delay in time (hours) for DIP intervention affects difference in time it takes for DIPs to reach half its steady state value for each organ.

Chapter 5

Epilogue

Control of infectious diseases has been a constant challenge throughout human history. Now, with antibiotic resistance and difficulties administering vaccinations, new and creative approaches must be taken. Mathematical modeling has played an important role in ensuring efficient implementation of control measures. In this dissertation, we looked at various diseases and control measures and how various mathematical models can be used to investigate the effectiveness of those control measures.

We first looked at how placing a quarantine on certain population compartments in an Ebola model (a disease where a vaccine is not available yet) affected the accuracy of the type of model used for that compartment. While delay differential equations can be more accurate, they tend to be more difficult to solve. Therefore, we found conditions when ordinary differential equations could be used instead. Using ODEs makes it easier to communicate results to policy makers, allowing for quick implementation of quarantine.

We then looked at how much yeast strains could benefit from expressing kin recognition in a biofilm formation through an agent-based stochastic spatial simulation. Since biofilms can cause infection and are difficult to remove with antibiotics, it is beneficial to investigate when biofilms can be disrupted through various social interactions among members of the community. We found that cooperators in a biofilm do benefit from expressing kin recognition and that they have more benefit when cooperators are less abundant with intermediate levels

of cooperation effect. Cooperators also had a higher benefit to expressing kin recognition in dense colonies.

Finally, we used a multiscale two-patch ordinary differential equations model for the competition between defective interfering particles and wild-type poliovirus spreading between two organs in a human host. Poliovirus is not yet extinct, and difficulties transporting vaccines and the high probability for the RNA virus to evolve from its attenuated strain makes it difficult to eradicate in some parts of the world. We found that DIPs are able to lower the WT population levels so that another intervention, such as the host's immune system, can more easily eliminate the virus.

These various scales and types of mathematical models allow us to investigate how well novel control methods will work. The use of multiscale models gives a better understanding of the biological workings of an infection and contributes to further accuracy of the model. By ensuring the accuracy, policy makers can be quickly convinced on the best control methods to implement, saving time and cost in the fight to control and prevent infectious disease.

Bibliography

- Anderson, R. M., R. M. May, and B. Anderson (1992). Infectious diseases of humans: dynamics and control, Volume 28. Wiley Online Library.
- Beretta, E. and D. Breda (2011). An SEIR epidemic model with constant latency time and infectious period. *Math Biosci Eng* 8(4): 931–952.
- Bird, S. W., N. D. Maynard, M. W. Covert, and K. Kirkegaard (2014). Nonlytic viral spread enhanced by autophagy components. *Proceedings of the National Academy of Sciences* 111(36): 13081–13086.
- Brandenburg, B., L. Y. Lee, M. Lakadamyali, M. J. Rust, X. Zhuang, and J. M. Hogle (2007). Imaging poliovirus entry in live cells. *PLoS biology* 5(7): e183.
- Brauer, F., C. Castillo-Chavez, and C. Castillo-Chavez (2001). *Mathematical models in population biology and epidemiology*, Volume 40. Springer.
- Brookmeyer, R., E. Johnson, and S. Barry (2005). Modelling the incubation period of anthrax. *Stat Med* 24(4): 531–542.
- Brown, S. P., S. A. West, S. P. Diggle, and A. S. Griffin (2009). Social evolution in microorganisms and a trojan horse approach to medical intervention strategies. *Philosophical Transactions of the Royal Society B: Biological Sciences* 364(1533): 3157–3168.
- Burrill, C. P., V. R. Strings, and R. Andino (2013). Poliovirus: generation, quantification, propagation, purification, and storage. *Current protocols in microbiology* 29(1): 15H–1.

- Cao, P. and D. Wall (2017). Self-identity reprogrammed by a single residue switch in a cell surface receptor of a social bacterium. *Proceedings of the National Academy of Sciences* 114(14): 3732–3737.
- Centers for Disease Control and Prevention (2014). Vaccine research will accelerate eradication of polio.
- Centers for Disease Control and Prevention (2018). Our history.
- Cooke, K., P. Van den Driessche, and X. Zou (1999). Interaction of maturation delay and nonlinear birth in population and epidemic models. *J Math Biol* 39(4): 332–352.
- Cox, D. R. and H. D. Miller (1965). *The theory of stochastic processes*. John Wiley & Sons.
- Dowdle, W. R. and M. E. Birmingham (1997). The biologic principles of poliovirus eradication. *The Journal of infectious diseases* 175(Supplement_1): S286–S292.
- Eichner, M. and K. Dietz (2003). Transmission potential of smallpox: estimates based on detailed data from an outbreak. *Am J Epidemiol* 158(2): 110–117.
- Feng, Z., D. Xu, and H. Zhao (2007). Epidemiological models with non-exponentially distributed disease stages and applications to disease control. *Bull Math Biol* 69(5): 1511–1536.
- Gardner, A. and S. A. West (2010). Greenbeards. *Evolution: International Journal of Organic Evolution* 64(1): 25–38.
- Gaynes, R. P. (2011). *Germ theory: medical pioneers in infectious diseases*. Am Soc Microbiol.
- Gilbert, N. (2008). *Agent-based models*. Number 153. Sage.
- Haas, C. N. (2014). On the quarantine period for Ebola virus. *PLoS Curr* 6.
- Hamilton, W. D. (1964). The genetical evolution of social behaviour. ii. *Journal of theoretical biology* 7(1): 17–52.

- Hethcote, H., M. Zhién, and L. Shengbing (2002). Effects of quarantine in six endemic models for infectious diseases. *Math Biosci* 180(1-2): 141–160.
- Hethcote, H. W. (2000). The mathematics of infectious diseases. *SIAM rev* 42(4): 599–653.
- Hirose, S., R. Benabentos, H.-I. Ho, A. Kuspa, and G. Shaulsky (2011). Self-recognition in social amoebae is mediated by allelic pairs of tiger genes. *Science* 333(6041): 467–470.
- Hu, K., S. Bianco, S. Edlund, and J. Kaufman (2015). The impact of human behavioral changes in 2014 West Africa Ebola outbreak. In *Social Computing, Behavioral-Cultural Modeling, and Prediction*, pp. 75–84. Springer.
- Huang, A. S. (1973). Defective interfering viruses. *Annual Reviews in Microbiology* 27(1): 101–118.
- Huang, A. S. and D. Baltimore (1970). Defective viral particles and viral disease processes. *Nature* 226(5243): 325.
- Huang, G., Y. Takeuchi, W. Ma, and D. Wei (2010). Global stability for delay SIR and SEIR epidemic models with nonlinear incidence rate. *Bull Math Biol* 72(5): 1192–1207.
- Kaddar, A., A. Abta, and H. T. Alaoui (2011). A comparison of delayed SIR and SEIR epidemic models. *Nonlinear Anal Model Control* 16(2): 181–190.
- Keeling, M. J. and B. T. Grenfell (2002). Understanding the persistence of measles: reconciling theory, simulation and observation. *Proc R Soc B* 269(1489): 335–343.
- Kermack, W. O. and A. G. McKendrick (1927). A contribution to the mathematical theory of epidemics. In *Proc R Soc A*, Volume 115, pp. 700–721. The Royal Society.
- Kew, O. M., R. W. Sutter, E. M. de Gourville, W. R. Dowdle, and M. A. Pallansch (2005). Vaccine-derived polioviruses and the endgame strategy for global polio eradication. *Annu. Rev. Microbiol.* 59: 587–635.

- Kim, W., F. Racimo, J. Schluter, S. B. Levy, and K. R. Foster (2014). Importance of positioning for microbial evolution. *Proceedings of the National Academy of Sciences* 111(16): E1639–E1647.
- Klasse, P. (2015). Molecular determinants of the ratio of inert to infectious virus particles. In *Progress in molecular biology and translational science*, Volume 129, pp. 285–326. Elsevier.
- Kuss, S. K., C. A. Etheredge, and J. K. Pfeiffer (2008). Multiple host barriers restrict poliovirus trafficking in mice. *PLoS pathogens* 4(6): e1000082.
- Leemis, L. (2011). *Probability*. Lightning Source.
- Li, M. and X. Liu (2014). An SIR epidemic model with time delay and general nonlinear incidence rate. In *Abstr Appl Analysis*, Volume 2014. Hindawi Publishing Corporation.
- Marriott, A. and N. Dimmock (2010). Defective interfering viruses and their potential as antiviral agents. *Reviews in medical virology* 20(1): 51–62.
- Meltzer, M. I. (2016). Modeling in real time during the Ebola response. *MMWR Suppl* 65.
- Meltzer, M. I., C. Y. Atkins, S. Santibanez, B. Knust, B. W. Petersen, E. D. Ervin, S. T. Nichol, I. K. Damon, M. L. Washington, et al. (2014). Estimating the future number of cases in the Ebola epidemic Liberia and Sierra Leone, 2014–2015. *MMWR Surveill Summ* 63(suppl 3): 1–14.
- Momeni, B., K. A. Briley, M. W. Fields, and W. Shou (2013). Strong inter-population cooperation leads to partner intermixing in microbial communities. *elife* 2: e00230.
- Murillo, L. N., M. S. Murillo, and A. S. Perelson (2013). Towards multiscale modeling of influenza infection. *Journal of theoretical biology* 332: 267–290.
- Nadell, C. D., K. Drescher, and K. R. Foster (2016). Spatial structure, cooperation and competition in biofilms. *Nature Reviews Microbiology* 14(9): 589.

- Nadell, C. D., K. R. Foster, and J. B. Xavier (2010). Emergence of spatial structure in cell groups and the evolution of cooperation. *PLoS computational biology* 6(3): e1000716.
- Nadell, C. D., J. B. Xavier, and K. R. Foster (2008). The sociobiology of biofilms. *FEMS microbiology reviews* 33(1): 206–224.
- Nishiura, H. (2007). Time variations in the transmissibility of pandemic influenza in Prussia, Germany, from 1918–19. *Theor Biol Med Model* 4(1): 20.
- Noh, S., K. S. Geist, X. Tian, J. E. Strassmann, and D. C. Queller (2018). Genetic signatures of microbial altruism and cheating in social amoebas in the wild. *Proceedings of the National Academy of Sciences* 115(12): 3096–3101.
- Pandey, A., K. E. Atkins, J. Medlock, N. Wenzel, J. P. Townsend, J. E. Childs, T. G. Nyenswah, M. L. Ndeffo-Mbah, and A. P. Galvani (2014). Strategies for containing Ebola in West Africa. *Sci* 346(6212): 991–995.
- Pfeiffer, J. K. (2010). Innate host barriers to viral trafficking and population diversity: lessons learned from poliovirus. In *Advances in virus research*, Volume 77, pp. 85–118. Elsevier.
- Pfeiffer, J. K. and K. Kirkegaard (2006). Bottleneck-mediated quasispecies restriction during spread of an RNA virus from inoculation site to brain. *Proceedings of the National Academy of Sciences* 103(14): 5520–5525.
- Racaniello, V. R. and D. Baltimore (1981). Molecular cloning of poliovirus cDNA and determination of the complete nucleotide sequence of the viral genome. *Proceedings of the National Academy of Sciences* 78(8): 4887–4891.
- Rast, L. I., I. M. Rouzine, G. Rozhnova, L. Bishop, A. D. Weinberger, and L. S. Weinberger (2016). Conflicting selection pressures will constrain viral escape from interfering particles: Principles for designing resistance-proof antivirals. *PLoS computational biology* 12(5): e1004799.

- Regoes, R. R., S. Crotty, R. Antia, and M. M. Tanaka (2005). Optimal replication of poliovirus within cells. *The American Naturalist* 165(3): 364–373.
- Rouzine, I. M. and L. S. Weinberger (2013). Design requirements for interfering particles to maintain coadaptive stability with hiv-1. *Journal of virology* 87(4): 2081–2093.
- Safi, M. A. and A. B. Gumel (2011). The effect of incidence functions on the dynamics of a quarantine/isolation model with time delay. *Nonlinear Anal RWA* 12(1): 215–235.
- Schulte, M. B. and R. Andino (2014). Single-cell analysis uncovers extensive biological noise in poliovirus replication. *Journal of virology*: JVI-03539.
- Shampine, L. F. and S. Thompson (2001). Solving ddes in Matlab. *Appl Numer Math* 37(4): 441–458.
- Sherborne, N., K. Blyuss, and I. Kiss (2015). Dynamics of multi-stage infections on networks. *Bull Math Biol* 77(10): 1909–1933.
- Sherman, I. W. (2007). *Twelve diseases that changed our world*. ASM Press Washington, DC.
- Shirogane, Y., E. Rousseau, J. Voznica, I. Rouzine, S. Bianco, and R. Andino (2019). Experimental and mathematical insights on the competition between poliovirus and a defective interfering genome. *bioRxiv*.
- Smukalla, S., M. Caldara, N. Pochet, A. Beauvais, S. Guadagnini, C. Yan, M. D. Vences, A. Jansen, M. C. Prevost, J.-P. Latgé, et al. (2008). Flo1 is a variable green beard gene that drives biofilm-like cooperation in budding yeast. *Cell* 135(4): 726–737.
- Stefanic, P., B. Kraigher, N. A. Lyons, R. Kolter, and I. Mandic-Mulec (2015). Kin discrimination between sympatric bacillus subtilis isolates. *Proceedings of the National Academy of Sciences* 112(45): 14042–14047.

- Strassmann, J. E., O. M. Gilbert, and D. C. Queller (2011). Kin discrimination and cooperation in microbes. *Annual review of microbiology* 65: 349–367.
- The Sage Developers (2018). SageMath, the Sage Mathematics Software System (Version x.y.z). <https://www.sagemath.org>.
- ThermoFisher Scientific (2019). Useful numbers for cell culture.
- Thompson, K. A. S. and J. Yin (2010). Population dynamics of an rna virus and its defective interfering particles in passage cultures. *Virology journal* 7(1): 257.
- Trono, D., R. Andino, and D. Baltimore (1988). An RNA sequence of hundreds of nucleotides at the 5'end of poliovirus RNA is involved in allowing viral protein synthesis. *Journal of virology* 62(7): 2291–2299.
- Van den Driessche, P. and J. Watmough (2002). Reproduction numbers and sub-threshold endemic equilibria for compartmental models of disease transmission. *Math Biosci* 180(1): 29–48.
- Van Gestel, J., F. J. Weissing, O. P. Kuipers, and A. T. Kovács (2014). Density of founder cells affects spatial pattern formation and cooperation in bacillus subtilis biofilms. *The ISME journal* 8(10): 2069.
- Vos, M. and G. J. Velicer (2009). Social conflict in centimeter-and global-scale populations of the bacterium myxococcus xanthus. *Current Biology* 19(20): 1763–1767.
- Waldman, B. (1988). The ecology of kin recognition. *Annual review of ecology and systematics* 19(1): 543–571.
- Washington, M. L. and M. L. Meltzer (2015). Effectiveness of ebola treatment units and community care centers-liberia, september 23-october 31, 2014. *MMWR. Morb Mortal Wkly Rep* 64(3): 67–69.

- Wearing, H. J., P. Rohani, and M. J. Keeling (2005). Appropriate models for the management of infectious diseases. *PLoS Med* 2(7): e174.
- West, S. A., S. P. Diggle, A. Buckling, A. Gardner, and A. S. Griffin (2007). The social lives of microbes. *Annu. Rev. Ecol. Evol. Syst.* 38: 53–77.
- West, S. A., A. S. Griffin, and A. Gardner (2007). Social semantics: altruism, cooperation, mutualism, strong reciprocity and group selection. *Journal of evolutionary biology* 20(2): 415–432.
- Wimmer, E., C. U. Hellen, and X. Cao (1993). Genetics of poliovirus. *Annual review of genetics* 27(1): 353–436.
- World Health Organization (2019a). History of WHO.
- World Health Organization (2019b). Poliomyelitis.
- Xavier, J. B. and K. R. Foster (2007). Cooperation and conflict in microbial biofilms. *Proceedings of the National Academy of Sciences* 104(3): 876–881.
- Yang, Y., D. Xu, and Z. Feng (2008). Analysis of a model with multiple infectious stages and arbitrarily distributed stage durations. *Math Model Nat Phenom* 3(07): 180–193.
- Zhang, J.-Z., Z. Jin, Q.-X. Liu, and Z.-Y. Zhang (2009). Analysis of a delayed SIR model with nonlinear incidence rate. *Discret Dyn Nat Soc* 2008.

Vita

Adrienna Bingham was born in San Angelo, Texas on December 22, 1991. She earned her Bachelors of Science degree in Mathematics from Angelo State University in May 2014 with minors in Computer Science and Spanish. She went on to get her Masters of Science degree in Applied Science from the College of William and Mary with a concentration in Mathematical and Computational Biology in January of 2016.